

# Using Linearized Optimal Transport to Predict the Evolution of Stochastic Particle Systems

Nicholas Karris<sup>1</sup>, Evangelos A. Nikitopoulos<sup>2</sup>, Ioannis Kevrekidis<sup>3</sup>, Seungjoon Lee<sup>4</sup>, and Alexander Cloninger<sup>5</sup>

<sup>1,5</sup>University of California, San Diego

<sup>2</sup>University of Michigan

<sup>3</sup>Johns Hopkins University

<sup>4</sup>California State University, Long Beach

January 9, 2025

## Abstract

We develop an algorithm to approximate the time evolution of a probability distribution without explicitly learning an operator that governs the evolution. A particular application of interest is discrete measures  $\mu_t^N$  that arise from systems of  $N$  particles in  $\mathbb{R}^d$ . In many such situations, the individual particles move chaotically on short time scales, making it difficult to learn the dynamics of a governing operator, but the bulk distribution  $\mu_t^N$  approximates an absolutely continuous measure  $\mu_t$  that evolves “smoothly.” If  $\mu_t$  is known on some time interval, then linearized optimal transport theory provides an Euler-like scheme for approximating the evolution of  $\mu_t$  using its “tangent vector field” (represented as a time-dependent vector field on  $\mathbb{R}^d$ ), which can be computed as a limit of optimal transport maps. We propose an analog of this Euler approximation to predict the evolution of the discrete measure  $\mu_t^N$  (*without* knowing  $\mu_t$ ). To approximate the analogous tangent vector field, we use a finite difference over a time step that sits between two time scales of the system — long enough for a large- $N$  evolution ( $\mu_t$ ) to emerge but short enough to satisfactorily approximate the derivative object used in the Euler scheme. The emergence of the limiting behavior ensures the optimal transport maps closely approximate the vector field describing the bulk distribution’s smooth evolution instead of the individual particles’ more chaotic movements. We demonstrate the efficacy of our approach with two illustrative examples, Gaussian diffusion and a cell chemotaxis model, and show that our method succeeds in predicting the bulk behavior over relatively large steps.

## 1 Introduction

In this paper, we focus on the problem of predicting the value of a time-dependent probability distribution  $\mu_t$  on  $\mathbb{R}^d$ , representing the distribution of some physical system, given only access to  $\mu_t$  at discrete times  $t_j = jh$  for some small time step  $h$  whose size we cannot control. Often, the physics governing the system can be viewed as an oracle operator  $E_h$  that takes as input the present state  $\mu_t$  of the system and returns its state  $E_h(\mu_t) = \mu_{t+h}$  after “evolving” according to the underlying dynamics for a short time  $h$ . A natural way to understand the physical system is to attempt to learn the operator  $E_h$ . Many approaches to learning operators focus on tracking

a sample of  $\mu_t$  through the actions of  $E_h$  and then interpolating the results [22, 13, 14, 24, 18]. However, in many applications, it is not possible to track the action of  $E_h$  on individual sample particles. This could be a byproduct of the method of accessing samples from  $\mu_t$  and  $\mu_{t+h}$  (e.g., one can only sample from each distribution independently) or because  $E_h$  is random, so tracking individual samples is statistically unreliable.

We consider a different perspective to solving this problem, where instead of learning the entire operator  $E_h$ , we ask whether it is possible to predict the measure evolution *without* needing to understand the underlying dynamics. Explicitly, given  $\mu_t$  and  $\mu_{t+h}$  (or finite samples from these distributions) for some small time step  $h$ , can we predict the measure  $\mu_{t+H}$  for a larger time step  $H$ ? Similarly, is there a way to produce a sample from the predicted distribution  $\mu_{t+H}$  without needing to reconstruct the distribution itself from summary statistics? If so, then we can build an Euler-like method for approximating the long-term evolution of the distribution by making successive approximations.

There are several potential approaches to this problem. One simple idea is to linearly approximate how the density at a few chosen points in the support of the distributions changes over time. Explicitly, if  $p_t$  is the probability density of  $\mu_t$ , then one could approximate

$$p_{t+H}(x) \approx p_t(x) + H \cdot \frac{p_{t+h}(x) - p_t(x)}{h},$$

where  $\frac{p_{t+h}(x) - p_t(x)}{h}$  acts as a finite difference approximation of the time derivative of  $p_t(x)$ . Performing this on sufficiently many points  $x$  and interpolating the results would give a reasonable way to approximate  $\mu_{t+H}$ . If instead we only have samples from  $\mu_t$  and  $\mu_{t+h}$ , we could first apply some kernel density estimation technique to approximate the density functions and then follow a similar approach. There are many other similar ideas, each with its own merits and drawbacks, which we detail in Section 2.3. One drawback common to most approaches in this style, though, is that they rely on computing summary statistics, predicting the summary statistics, and reconstructing a distribution with the predicted statistics. We seek an approach that avoids the use of summary statistics and instead directly uses the measure-valued data to predict  $\mu_{t+H}$ . To do this, we need a metric  $D$  on the space of Borel probability distributions  $\mathcal{P}(\mathbb{R}^d)$  with the following properties:

- $t \mapsto \mu_t$  is continuous with respect to  $D$ , i.e.,  $D(\mu_t, \mu_{t+h}) \rightarrow 0$  as  $h \rightarrow 0$ .
- The space  $\mathcal{P}(\mathbb{R}^d)$ , or some subset, can be (formally) interpreted as a Riemannian manifold with Riemannian distance function  $D$ .
- If  $t \mapsto \mu_t$  is “differentiable,” then we can compute a tangent vector field to use in an analog of Euler’s method on  $\mathcal{P}(\mathbb{R}^d)$  to forecast  $\mu_{t+H}$ .
- Computing the distance between discrete measures does not require estimating any densities.

The Wasserstein distance  $W_2$  from optimal transport is a perfect candidate. By endowing the space of probability measures (with finite second moment) with the (2-)Wasserstein distance, we can view the evolution of  $\mu_t$  as a curve on the Wasserstein manifold  $\mathcal{P}_2(\mathbb{R}^d)$  [1, 21]. The measure-valued analog of a linear approximation, then, is to approximate future values  $\mu_{t+H}$  using the geodesic passing through  $\mu_t$  in the direction of  $\mathbf{v}_t$ , the tangent vector to the curve at  $\mu_t$ . In the language of differential geometry, we apply the exponential map to  $H\mathbf{v}_t$ . In linearized optimal transport

theory, the tangent space space of  $\mathcal{P}_2(\mathbb{R}^d)$  at  $\mu_t$  is described as a subspace of  $L^2(\mathbb{R}^d, \mu_t; \mathbb{R}^d)$  in such a way that

$$\nu \mapsto T_{\mu_t}^\nu - \text{id}_{\mathbb{R}^d}$$

is the inverse of the exponential map at  $\mu_t$ , where  $T_{\mu_t}^\nu$  is the optimal transport map from  $\mu_t$  to  $\nu$  [12, 23]. Thus, the tangent vector field  $\mathbf{v}_t$  should be given by

$$\mathbf{v}_t = \lim_{h \rightarrow 0} \frac{(T_{\mu_t}^{\mu_{t+h}} - \text{id}) - (T_{\mu_t}^{\mu_t} - \text{id})}{h} = \lim_{h \rightarrow 0} \frac{T_{\mu_t}^{\mu_{t+h}} - \text{id}}{h}.$$

It is known (see Theorem 4.6) that if  $t \mapsto \mu_t$  is “smooth” enough, then the limit above exists in  $L^2(\mathbb{R}^d, \mu_t; \mathbb{R}^d)$  and is the unique “minimal energy” vector field  $\mathbf{v}_t$  that satisfies the continuity equation

$$\partial_t \mu_t + \nabla \cdot (\mathbf{v}_t \mu_t) = 0.$$

More simply, this vector field exactly describes the “flow of mass” of the evolving measure. The key insight is that by fixing the reference measure  $\mu_t$ , we can use optimal transport maps from  $\mu_t$  to  $\mu_{t+h}$  for small values of  $h$  to understand where each infinitesimal piece of mass of  $\mu_t$  is moving. Moreover, interpreting  $\mathbf{v}_t$  as the tangent vector field to the curve  $(\mu_t)_{t \geq 0}$  on the Wasserstein manifold, the same results show that the geodesic in the direction of  $\mathbf{v}_t$  starting at  $\mu_t$  is a first-order accurate approximation of the true curve [2, 28]. This suggests that the measure-valued analog of Euler’s method is a first-order method for approximating a curve of measures evolving according to a prescribed vector field, which we show (under appropriate hypotheses) in Theorem 4.1. We then use this analogy to motivate an Euler-inspired algorithm for approximating the evolution of a measure: If we can query an oracle that takes as input a measure  $\mu_t$  at time  $t$  and returns  $E_h(\mu_t) = \mu_{t+h}$ , the measure that would result if  $\mu_t$  were allowed to evolve according to the underlying dynamics for a small time step  $h$ , then we can use this to approximate the tangent vector field  $\mathbf{v}_t$  by

$$\mathbf{v}_t^h := \frac{T_{\mu_t}^{E_h(\mu_t)} - \text{id}}{h} = \frac{T_{\mu_t}^{\mu_{t+h}} - \text{id}}{h}.$$

We can then use this approximation as the tangent vector in an Euler step. Iterating this process for successive approximations gives an Euler-like method for approximating the evolution of a measure without attempting to learn anything about the operator  $E_h$ .

A key feature of this approach is that it can be formulated in “discrete” cases. In this paper, we specifically consider cases arising from particle systems. Let  $x_1(t), \dots, x_N(t)$  be a system of  $N$  (random) particles in  $\mathbb{R}^d$  evolving in time, and define  $\mu_t^N := N^{-1} \sum_{i=1}^N \delta_{x_i(t)}$ . If  $\nu := \mu_t^N$  and  $\rho := \mu_{t+h}^N$ , then the Euler-like method described above becomes the following algorithm:

1. Compute a (discrete) optimal transport plan from  $\nu$  to  $\rho$  (using squared Euclidean distance as cost), and compute the barycentric projection to obtain a map  $T$ .
2. Use the map from Step 1 to form the difference quotient  $\mathbf{v}_t^h := \frac{T - \text{id}}{h}$ .
3. For each point in the support of  $\nu$ , take an Euler step using its current location and the velocity given by the “optimal transport vector field”  $\mathbf{v}_t^h$ .
4. Set  $\tilde{\mu}_{t+H}^N$  to be the uniform distribution on the points obtained by performing the Euler step from Step 3 on each point in the support of  $\nu$ .

5. Repeat Steps 1–4 using  $\tilde{\mu}_{t+H}^N$  as the “initial measure”  $\nu$ .

At this point, it is important to highlight that both regularity properties demanded of  $\mu_t$  in the earlier discussion of  $\mathbf{v}_t$  are generally false for  $\mu_t^N$ . Certainly,  $\mu_t^N$  does not have a density. Moreover,  $\mu_t^N$  can fail to be “smooth” because the particles may evolve chaotically. For example, if  $x_1, \dots, x_N$  are Brownian motions, then the sample paths are nowhere differentiable. Thus, there is no vector field locally describing the flow of the measure  $\mu_t^N$  and no tangent vector to the curve on the Wasserstein manifold, so the analog of Euler’s method does not work. This means that, *a priori*, it is not clear the algorithm above actually works in this setting. In many systems of interest, however, there is a “smooth” curve  $t \mapsto \mu_t$  of absolutely continuous measures such that “ $\mu_t^N \approx \mu_t$ ” for large  $N$ . (This happens, for example, if we start with the curve  $\mu = (\mu_t)_{t \geq 0}$  and the  $x_i$ s are i.i.d. samples of  $\mu$ .) For certain such systems, we experimentally demonstrate that the optimal transport–based algorithm described above can be used to give a good approximation of the state of the particle system at time  $t + H$ , where  $H \gg h$ , based only on data from times  $t$  and  $t + h$ .

One setting in which this approximation algorithm is particularly useful is if we have a micro-scale particle simulation  $E_h$ . Then we can think of  $\mu_t^N$  as the locations of the particles at time  $t$  and  $\mu_{t+h}^N$  is their locations at the “next time step” in the simulation. The benefit of accurately predicting  $\mu_{t+H}^N$  for a substantial time step  $H \gg h$  is that one can then skip (potentially many) micro-scale steps in the simulation and still understand how  $\mu_t^N$  evolves in time. Indeed, after predicting  $\mu_{t+H}^N$ , one can reinitialize the simulation with particles at those locations, take another small step in the simulation to obtain an estimate for  $\mu_{t+H+h}^N$ , and use the prediction algorithm again to approximate  $\mu_{t+2H}^N$ . (This is why it is important to have a natural way to produce a sample from the predicted measure.) Following strategies of some projective integration techniques [9, 29], doing this successively gives an Euler-like method for approximating the system’s behavior for a long time without the need to perform as many micro-scale steps. If the simulation is computationally expensive to perform, or if many particles and small time steps are required to observe the long-term behavior of interest, then having a way to reduce the number of micro-scale time steps could yield significant computational speed improvements.

## 1.1 Motivating Example

One particular class of particle systems of interest is so-called “fast-slow” systems [8, 17, 9, 29]. The key feature of such systems that makes them difficult to analyze is that there are multiple underlying variables that impact the particles’ behavior yet update on vastly different time scales. This means a micro-scale simulation must be run with small time steps to capture the “fast” dynamics accurately, but the “slow” dynamics manifest on time scales many orders of magnitude longer. Thus, accurate simulation requires many time steps to exhibit the desired behavior of the overall evolution of the bulk distribution of particles.

While these “fast-slow” dynamics refer to underlying data of the particles and not to the particles’ movement itself, they do have observable effects on the particles’ behavior. In general, the “fast” dynamics manifest in the particles behaving fairly chaotically on short time scales. For example, a particle may change direction many times as some of its underlying data fluctuate quickly based on interactions with nearby particles, but quickly after initializing the system, these data will reach a relative equilibrium that depends on the location of the particle and the density of particles at that location. In contrast, the “slow” dynamics manifest in the particles slowly demonstrating a

collective behavior (for example, cells migrating towards a higher concentration of a food source). The underlying data associated with this slower behavior take much longer to equilibrate, and they are often correlated more closely with the long-term motion of the particles in bulk.

A different class of particle systems that exhibit similar behavior is systems arising from the numerical solution of SDEs (e.g., Euler–Maruyama simulations). While this class is distinct from fast-slow systems, the stochastics introduce a similar dichotomy of two time scales. The individual particles behave chaotically on short time scales (indeed, the paths traced out by true solutions to SDEs are nowhere differentiable), yet it is possible to still have predictable behavior on much longer time scales (e.g., convergence to a steady state). For simplicity in this paper, and in order to highlight the important aspects of the prediction algorithm without getting caught up in the details of “fast-slow” systems, we will work primarily with these “stochastic” particle systems. In doing this, we are effectively making the simplifying assumption that these two types of particle systems present similar challenges to our prediction model: both systems yield a collective long-term evolution that, on short time scales, is masked by the particles’ unpredictable behavior. This means we can evaluate the efficacy of our proposed prediction algorithm by observing how well it performs on stochastic particle systems, which are easier to simulate and understand. In particular, micro-scale simulations for stochastic systems are often computationally cheap, which allows us to easily compare our predictions with the “true” evolution of the system.

The stochastic particle system example is a particularly useful one to consider because it also nicely demonstrates some of the subtlety of applying the prediction algorithm to discrete distributions. For absolutely continuous measures, the optimal transport approach works well because it accurately approximates the vector field that describes the flow of the measure over time. To understand why the case of discrete measures is more complicated, we recall that for two uniform measures on the same (finite) number of points, the optimal transport plan between them is a permutation (and the Barycentric projection is trivial) [27]. Thus, if each particle is evolving continuously in time, then for a small enough time step  $h$ , the optimal transport map between  $\mu_t^N$  and  $\mu_{t+h}^N$  is exactly the identity permutation. This means the associated vector field describes the movement of the particles, which in the case of stochastic particle systems is chaotic and unstructured on small time scales. It says nothing about how the bulk distribution of particles is evolving. In order for the optimal transport map to capture the structure of the bulk evolution, the time difference  $h$  must be sufficiently long that the optimal transport map is no longer the identity permutation, i.e., that the particles have “mixed” themselves well enough. This sufficiently long time allows for the long-term bulk behavior to begin to overshadow the effects of the short-term chaotic particle behavior, consequently allowing the optimal transport map to capture the bulk behavior of interest.

However, the goal of computing the optimal transport map is to approximate a tangent vector, and we need a short time step for the finite difference approximation of the tangent vector to be accurate. These competing desires mean that choosing an appropriate length of time for the finite difference is delicate; we need it to be long enough that the optimal transport map reveals the bulk behavior but still short enough to closely approximate the correct vector field. This is intuitively possible to do for systems where the two time scales are vastly different, but determining when this actually happens is less clear theoretically.

Reliably finding an appropriate time step to balance these two competing desires is a subject of active study in multiscale modeling (see Section 2.3). We will, however, experimentally verify that

if the particles give an empirical estimate of a true distribution that is evolving smoothly, then for a well chosen time step, the discrete optimal transport map approximates the vector field that describes the true distribution’s evolution. We also observe that the time scales required for the bulk behavior to emerge are very short compared to the overall evolution of the distribution. This means it is indeed possible to choose a time step for the finite difference that balances the two time scales and also that there are still speed improvements to be gained by using the Euler-like approximation scheme. We then demonstrate that the prediction algorithm using this vector field works well in some model examples of particle systems, suggesting that the results for continuous measures may extend to the discrete case.

## 1.2 Major Contributions

In this paper, we make the following contributions:

- We relate Euler’s method to the study of linearized optimal transport and the geometry of the Wasserstein manifold (Section 4.1).
- We describe an analog of Euler’s method for approximating measure-valued solutions to the continuity equation with prescribed velocity field flows (Section 4.2).
- We prove that, under sufficient regularity conditions, this method with step size  $H$  has local truncation error  $\mathcal{O}(H^2)$  and corresponding global error  $\mathcal{O}(H)$  (Theorems 4.1 and 4.16).
- We detail an algorithm that uses linearized optimal transport to approximate the evolution of discrete particle systems, and we note how it is analogous to the theory that already exists for measures with densities (Section 5).
- We demonstrate both the benefit of using optimal transport (versus using individual particles, Section 6.2) and also the computational benefit of our approximation algorithm (Section 6.1).
- We apply our approximation algorithm to bacterial chemotaxis as described in [29] (Section 7).

## 2 Background

### 2.1 Optimal Transport Preliminaries

Let  $\mathcal{P}(\mathbb{R}^d)$  be the set of Borel probability measures on  $\mathbb{R}^d$  and let  $\mathcal{P}_2(\mathbb{R}^d)$  be the set of measures  $\mu \in \mathcal{P}(\mathbb{R}^d)$  such that  $\int_{\mathbb{R}^d} \|x\|_2^2 d\mu(x) < \infty$ . For a measurable function  $T : \mathbb{R}^d \rightarrow \mathbb{R}^d$  and a measure  $\sigma \in \mathcal{P}(\mathbb{R}^d)$ , the pushforward of  $\sigma$  by  $T$  is the measure  $T_{\#}\sigma$  defined by

$$(T_{\#}\sigma)(A) := \sigma(T^{-1}(A))$$

where  $A \subset \mathbb{R}^d$  is measurable and  $T^{-1}(A)$  is the preimage of  $A$  under  $T$ .

Given  $\sigma, \mu \in \mathcal{P}_2(\mathbb{R}^d)$ , a classical problem is to seek a map  $T$  transporting  $\sigma$  to  $\mu$  in the sense that  $T_{\#}\sigma = \mu$ . Below is a fundamental result in optimal transport theory that provides existence and uniqueness of “optimal” such  $T$ .

**Theorem 2.1** (Brenier [4]). *Let  $\sigma, \mu \in \mathcal{P}_2(\mathbb{R}^d)$ , and suppose at least one of  $\sigma, \mu$  has a density with respect to the Lebesgue measure  $\mathcal{L}^d$ . There exists a  $\sigma$ -a.e. unique map  $T : \mathbb{R}^d \rightarrow \mathbb{R}^d$  that solves the*

optimization problem

$$\inf_{\{S: S_{\#}\sigma=\mu\}} \int_{\mathbb{R}^d} \|x - S(x)\|_2^2 d\sigma(x). \quad (2.2)$$

Moreover, there exists a convex function  $\phi : \mathbb{R}^d \rightarrow \mathbb{R}$ , unique up to an additive constant, such that  $T = \nabla\phi$ .

**Definition 2.3.** The map  $T$  given in Theorem 2.1 is the *optimal transport map* from  $\sigma$  to  $\mu$ , and we denote it  $T_{\sigma}^{\mu}$ .

The square root of the number in (2.2) is the (2-)Wasserstein distance between  $\sigma$  and  $\mu$  and is denoted  $W_2(\sigma, \mu)$ , i.e.,

$$W_2(\sigma, \mu) = \left( \inf_{\{S: S_{\#}\sigma=\mu\}} \int_{\mathbb{R}^d} \|x - S\|_2^2 d\sigma(x) \right)^{\frac{1}{2}}.$$

It is well known that  $W_2$  defines a metric on  $\mathcal{P}_2(\mathbb{R}^d)$  (see, e.g., [27]).

Optimal transport is also possible between discrete measures. In general, this requires solving a more general optimization problem (the Kantorovich relaxation), but the following result guarantees that (2.2) is solvable in the case of uniform measures on the same finite number of points.

**Proposition 2.4** (e.g., Proposition 2.1 in [27]). *If  $\sigma = \frac{1}{N} \sum_{i=1}^N \delta_{x_i}$  and  $\mu = \frac{1}{N} \sum_{i=1}^N \delta_{y_i}$  are uniform measures on the same number of points, then there exists an optimal transport map  $T_{\sigma}^{\mu}$  solves (2.2) (and also the Kantorovich relaxation).*

Unlike in Theorem 2.1, the optimal transport map given by Proposition 2.4 is not necessarily unique, even  $\sigma$ -a.e. In this discrete case, the notation  $T_{\sigma}^{\mu}$  will denote a particular choice of an optimal map.

## 2.2 Linearized Optimal Transport

As Otto first observed in [26],  $\mathcal{P}_2(\mathbb{R}^d)$  has a kind of “infinite-dimensional Riemannian manifold” structure. Because of this, the language of differential geometry is often used, although the analogy is typically more formal than precise. The key example of interest for us is the description of the “tangent bundle” of the Wasserstein manifold  $\mathbb{W}_2$ . One can show that for measures  $\mu_0, \mu_1 \in \mathcal{P}_2(\mathbb{R}^d)$ , the curve

$$t \mapsto \mu_t := ((1-t)\text{id} + tT_{\mu_0}^{\mu_1})_{\#}\mu_0$$

is the constant-speed geodesic in  $W_2$  from  $\mu_0$  to  $\mu_1$  (see, e.g., Section 7.2 of [2]). Furthermore, it can be shown (e.g., in Section 5.4 of [28]) that the vector field

$$\mathbf{v}_t(x) := (T_{\mu_0}^{\mu_1} - \text{id}) \left( ((1-t)\text{id} + tT_{\mu_0}^{\mu_1})^{-1}(x) \right)$$

is the Benamou–Brenier velocity field associated to the geodesic  $\mu_t$  [3]. In this way, we can think of  $\mathbf{v}_0 = T_{\mu_0}^{\mu_1} - \text{id} \in L^2(\mathbb{R}^d, \mu_0; \mathbb{R}^d)$  as the “tangent vector” to the geodesic between  $\mu_0$  and  $\mu_1$  at the point  $\mu_0$ . Accordingly, it is reasonable to view the tangent space  $T_{\mu_0}\mathbb{W}_2$  as (a subspace of)  $L^2(\mathbb{R}^d, \mu_0; \mathbb{R}^d)$  and the logarithm map, i.e., the inverse of the exponential map, at  $\mu_0$  as the map

$$\log_{\mu_0}^{\mathbb{W}_2} : \mathbb{W}_2 \rightarrow T_{\mu_0}\mathbb{W}_2, \quad \log_{\mu_0}^{\mathbb{W}_2}(\mu_1) = \mathbf{v}_0.$$

This tangent space is discussed more in Section 4.1; see also [1] for a more detailed discussion. Thus, we can use the embedding  $\mu_1 \mapsto T_{\mu_0}^{\mu_1} - \text{id}$  to “linearize” the space of measures. Specifically, for a fixed reference measure  $\sigma \in \mathcal{P}_2(\mathbb{R}^d)$ , we can use the map

$$\mu \mapsto T_{\sigma}^{\mu} - \text{id}$$

to embed probability measures in the linear space  $L^2(\mathbb{R}^d, \sigma; \mathbb{R}^d)$ . We can then define the LOT (linearized optimal transport) [32] distance between two measures  $\mu, \nu$  by

$$W_{2,\sigma}^{LOT}(\mu, \nu) := \|(T_{\sigma}^{\mu} - \text{id}) - (T_{\sigma}^{\nu} - \text{id})\|_{L^2(\sigma)} = \|T_{\sigma}^{\mu} - T_{\sigma}^{\nu}\|_{L^2(\sigma)}.$$

By a simple change of variables, we immediately get the inequality

$$W_2(\mu, \nu) \leq W_{2,\sigma}^{LOT}(\mu, \nu).$$

The reverse inequality exists with different levels of sharpness depending on assumptions on the distributions; [12, 23] both give a bi-Hölder equivalence for different Hölder constants under different assumptions. There are many advantages to this linear embedding; see, for example, [32, 25] for computational speedup and supervised learning and [5] for performing PCA.

### 2.3 Related Works

The relationship between linearized optimal transport and time-dependent measures has been explored before. [20] showed that under certain conditions on how the  $\mu_t$  are constructed, we can conclude that the map  $t \mapsto T_{\sigma}^{\mu_t}$  is of bounded variation in  $L^2(\sigma)$ . Then in [12], Gigli shows that if  $\sigma$  is arbitrary, then for any absolutely continuous curve  $t \mapsto \mu_t$ , the map  $t \mapsto T_{\sigma}^{\mu_t}$  is at most  $\frac{1}{2}$ -Hölder continuous. Based on Gigli’s hypotheses, we conclude that our only hope is to choose the reference measure to be  $\sigma = \mu_0$ , so that  $T_{\sigma}^{\mu_t} \rightarrow \text{id}$  in  $L^p(\mu_0)$  as  $t \rightarrow 0^+$ .

More generally, many different approaches have been explored for understanding fast-slow dynamical systems. A few examples of so-called “multi-scale methods” are presented in [17, 16, 11, 31, 7, 6], and other “projective integration methods” are proposed in [9, 8] and others. The techniques of Neural ODEs and Continuous Normalizing Flows can also be used to understand similar problems, for example in [15, 30]. However, each of these techniques relies on the particle systems coming from a (potentially very large but still) specific class of problems. In contrast, the method we propose only assumes that there is a global behavior to be found in the first place, i.e., that the true bulk distribution is evolving according to *some* velocity field flow. The goal of all of these methods is to somehow approximate that governing velocity field, and the method we describe is just one such approach. Our goal in presenting this method is not necessarily to outperform the other methods numerically or computationally, but rather to present an approach that naturally falls out of the theory. Because of this, we will not spend much time comparing our experimental results to methods like Neural ODEs or CNFs, but instead we draw broader conclusions about the efficacy and interpretability of our proposed algorithm.

## 3 Euler-like Methods with Imperfect Information

Before we discuss our method for approximating the evolution of particle distributions, it is helpful to understand the analog of our method in the context of a single particle evolving in  $\mathbb{R}^d$ . To do

this, suppose we have a particle whose location at time  $t$  is described by some curve  $\gamma(t)$ , and that  $\gamma$  solves the IVP

$$\gamma(0) = x_0, \quad \gamma'(t) = f(t, \gamma(t)).$$

Our goal is to numerically estimate  $\gamma(T)$  for some large  $T$ . If we happen to have access to the underlying “dynamics” function  $f$ , then we can use ordinary Euler’s method: for a time step  $H > 0$  and discrete times  $t_n = nH$ , approximate  $\gamma(t_n) \approx \gamma_{(n)}$ , where  $\gamma_{(n)}$  is defined recursively by

$$\gamma_{(0)} = x_0, \quad \gamma_{(n+1)} = \gamma_{(n)} + Hf(t_n, \gamma_{(n)}).$$

Under sufficient regularity conditions on  $f$ , it is well known that this is a first-order accurate numerical method.

However, in our context, we will not have explicit access to the underlying function  $f$ , so we cannot perform Euler’s method exactly. Instead, we will have access to some oracle  $E_h$  that, given a time  $t$  and a particle location  $\gamma$ , will return an approximation of where that particle would be at time  $t+h$  for some small time step  $h > 0$ . (For us, this oracle will be a micro-scale numerical simulation that is only accurate for very small time steps  $h$  and is computationally expensive to compute, so using it to simulate long-term behavior is impractical.) Given this information, we can then attempt to approximate  $f(t, \gamma)$  by

$$f(t, \gamma) \approx \frac{E_h(t, \gamma) - \gamma}{h} =: \hat{f}(t, \gamma).$$

Using this approximation, we can then define the Euler-like method

$$\gamma_{(0)} = x_0, \quad \gamma_{(n+1)} = \gamma_{(n)} + H \cdot \frac{E_h(t_n, \gamma_{(n)}) - \gamma_{(n)}}{h} = \gamma_{(n)} + H\hat{f}(t_n, \gamma_{(n)}).$$

The approximation algorithm we describe in Section 5 is the measure-valued analog of this Euler-like method, where  $E_h$  is a given micro-scale simulator.

This discussion naturally points to a broader class of Euler-like methods that use some approximation  $\hat{f}$  rather than  $f$  itself. It is not surprising that the error of these methods depends on how well  $\hat{f}$  approximates  $f$ , and while precise statements can be made, we omit the details for brevity. The informal statement is that if  $\hat{f}(t_n, \gamma_{(n)})$  well approximates  $f(t_n, \gamma_{(n)})$  for all  $n$ , then  $\gamma_{(n)}$  well approximates  $\gamma(t_n)$ .

**Remark 3.1.** As a bit of foreshadowing, note that Euler’s method may be written simply in terms of the exponential map on Euclidean space as

$$\gamma_{(n+1)} = \gamma_{(n)} + Hf(t_n, \gamma_{(n)}) = \exp_{\gamma_{(n)}}^{\mathbb{R}^d}(Hf(t_n, \gamma_{(n)})).$$

At its core, this means that Euler’s method approximates the true solution  $\gamma(t)$  with a series of geodesics (lines) in  $\mathbb{R}^d$ .

## 4 Measure-Valued Euler-Like Methods

To properly motivate our approximation algorithm, which will be an Euler-like method with an approximated tangent vector as described in the previous section, we must first know that Euler’s method with the true tangent vector works at all on the Wasserstein manifold. Thus, the main goal of this section is to motivate and prove the following result:

**Theorem 4.1.** *Let  $F : [0, T] \times \mathcal{P}_2(\mathbb{R}^d) \rightarrow (\mathbb{R}^d)^{\mathbb{R}^d} = \{\text{functions } \mathbb{R}^d \rightarrow \mathbb{R}^d\}$  be a map such that for all times  $t \in [0, T]$  and all measures  $\mu \in \mathcal{P}_2(\mathbb{R}^d)$ , the vector field  $F(t, \mu)$  is in  $T_\mu \mathbb{W}_2$  (defined in Theorem 4.2). Suppose  $F$  satisfies the following Lipschitz conditions: There exist  $L_1, L_2 \geq 0$  such that for all  $t \in [0, T]$ ,  $x_1, x_2 \in \mathbb{R}^d$ , and  $\mu_1, \mu_2 \in \mathcal{P}_2(\mathbb{R}^d)$ ,*

$$\begin{aligned} \|F(t, \mu)(x_1) - F(t, \mu)(x_2)\|_2 &\leq L_1 \|x_1 - x_2\|_2, & \text{and} \\ \|F(t, \mu_1) - F(t, \mu_2)\|_{L^2(\mu_i)} &\leq L_2 W_2(\mu_1, \mu_2) \quad (i = 1, 2). \end{aligned}$$

*Also, suppose there is an absolutely continuous curve  $\mu : [0, T] \rightarrow \mathcal{P}_2(\mathbb{R}^d)$ , written as  $t \mapsto \mu_t$ , that satisfies the continuity equation*

$$\partial_t \mu_t + \nabla \cdot (F(t, \mu_t) \mu_t) = 0$$

*in the sense of distributions, and that the function  $(t, x) \mapsto \mathbf{v}_t(x) := F(t, \mu_t)(x)$  is (jointly)  $C^1$ .*

*Then for  $\mu_0$ -a.e.  $x \in \mathbb{R}^d$ , the characteristic ODE*

$$\gamma_x(0) = x, \quad \frac{d}{dt} \gamma_x(t) = \mathbf{v}_t(\gamma_x(t))$$

*admits a unique  $C^2$  solution. Furthermore, if*

$$M := \left( \int_{\mathbb{R}^d} \max_{r \in [0, T]} \|\gamma_x''(r)\|_2^2 d\mu_0(x) \right)^{1/2} < \infty,$$

*then for a time step  $H > 0$  and discrete times  $t_n := nH$ , the sequence of Euler approximations iteratively defined by*

$$\mu_{(0)} := \mu_0, \quad \mu_{(n+1)} := (\text{id} + HF(t_n, \mu_{(n)}))\# \mu_{(n)}$$

*satisfies*

$$W_2(\mu_{(n)}, \mu_{t_n}) \leq \frac{HM}{2(L_1 + L_2)} \left( e^{nH(L_1 + L_2)} - 1 \right).$$

## 4.1 Tangent Fields of Curves on the Wasserstein Manifold

To begin this discussion, we first need to establish a reasonable notion of the derivative of a curve of measures. To this end, we cite the following result, which says that absolutely continuous curves on the Wasserstein manifold can be understood to be evolving according to a vector field flow at almost every time. This should be seen as analogous to the fundamental theorem of calculus for absolutely continuous curves in  $\mathbb{R}^d$ .

**Theorem 4.2** (Theorem 8.3.1 and Proposition 8.4.5 in [2]). *Let  $\mu : [0, T] \rightarrow \mathcal{P}_2(\mathbb{R}^d)$  be an absolutely continuous curve on  $\mathbb{W}_2 := (\mathcal{P}_2(\mathbb{R}^d), W_2)$ , and let  $|\mu'| (t)$  be its metric derivative. There exists a Borel vector field  $(t, x) \mapsto \mathbf{v}_t(x) \in \mathbb{R}^d$  such that*

$$\|\mathbf{v}_t\|_{L^2(\mu_t)} := \left( \int_{\mathbb{R}^d} \|\mathbf{v}_t(x)\|_2^2 d\mu_t(x) \right)^{1/2} \leq |\mu'| (t) \quad \text{for } \mathcal{L}^1\text{-a.e. } t \in (0, T) \quad (4.3)$$

*and the continuity equation*

$$\partial_t \mu_t + \nabla \cdot (\mathbf{v}_t \mu_t) = 0 \quad (4.4)$$

holds in the sense of distributions, i.e.,

$$\int_0^T \int_{\mathbb{R}^d} [\partial_t \phi(x, t) + \langle \mathbf{v}_t(x), \nabla_x \phi(x, t) \rangle] d\mu_t(x) dt = 0 \quad \text{for all } \phi \in C_c^\infty(\mathbb{R}^d \times (0, T)). \quad (4.5)$$

The map  $t \mapsto \mathbf{v}_t$  is  $\mathcal{L}^1$ -a.e. uniquely determined by (4.3) and (4.4). Now, for  $\nu \in \mathcal{P}_2(\mathbb{R}^d)$ , define  $T_\nu \mathbb{W}_2$  to be the closure in  $L^2(\mathbb{R}^d, \nu; \mathbb{R}^d)$  of  $\{\nabla \phi : \phi \in C_c^\infty(\mathbb{R}^d)\}$ . If  $\mathbf{v}$  is a Borel vector field satisfying (4.4), then (4.3) is satisfied if and only if  $\mathbf{v}_t \in T_{\mu_t} \mathbb{W}_2$  for  $\mathcal{L}^1$ -a.e.  $t \in [0, T]$ .

We now state the driving result of the paper, which says that the vector field given in Theorem 4.2 is computable as a derivative involving optimal transport maps:

**Theorem 4.6** (Proposition 8.4.6 in [2]). *Let  $\mu : [0, T] \rightarrow \mathcal{P}_2(\mathbb{R}^d)$  be an absolutely continuous curve, and let  $\mathbf{v}_t$  be the vector field provided by Theorem 4.2. For  $\mathcal{L}^1$ -a.e.  $t \in [0, T]$ ,*

$$\lim_{h \rightarrow 0} \frac{W_2(\mu_{t+h}, (\text{id} + h\mathbf{v}_t)_\# \mu_t)}{|h|} = 0. \quad (4.7)$$

In particular, if  $\mu_t \ll \mathcal{L}^d$  for all  $t \in [0, T]$ , then for  $\mathcal{L}^1$ -a.e.  $t \in [0, T]$ ,

$$\lim_{h \rightarrow 0} \frac{1}{h} (T_{\mu_t}^{\mu_{t+h}} - \text{id}) = \mathbf{v}_t \quad \text{in } L^2(\mathbb{R}^d, \mu_t; \mathbb{R}^d), \quad (4.8)$$

where  $T_{\mu_t}^{\mu_{t+h}}$  is the optimal transport map from  $\mu_t$  to  $\mu_{t+h}$ .

**Remark 4.9.** As a direct analog of Remark 3.1, we translate this into the language of differential geometry. For a point  $\mu \in \mathcal{P}_2(\mathbb{R}^d)$ , the Wasserstein manifold's exponential map at  $\mu$  is given by [1]

$$\exp_\mu^{\mathbb{W}_2} : T_\mu \mathbb{W}_2 \rightarrow \mathcal{P}_2(\mathbb{R}^d) \quad \exp_\mu^{\mathbb{W}_2}(\mathbf{v}) = (\text{id} + \mathbf{v})_\# \mu.$$

This notation is appropriate because the curve  $t \mapsto \exp_\mu^{\mathbb{W}_2}(t\mathbf{v})$  is a constant-speed geodesic on a small interval  $(-\varepsilon, \varepsilon)$ . Thus, the approximation of  $\mu_{t+h}$  suggested by Theorem 4.6 can be interpreted as applying the exponential map to the scaled tangent vector  $h\mathbf{v}_t$ :

$$\mu_{t+h} \approx (\text{id} + h\mathbf{v}_t)_\# \mu_t = \exp_{\mu_t}^{\mathbb{W}_2}(h\mathbf{v}_t).$$

Thus, this is the natural analog to a ‘‘linear approximation’’ of a curve on the Wasserstein manifold.

## 4.2 Euler's Method on the Wasserstein Manifold

The previous section's characterization of tangent fields to curves on the Wasserstein manifold motivates the following Wasserstein analog of Euler's method. The analog of approximating a solution to an ODE is approximating a solution to the continuity equation with specified velocity fields, i.e., to approximate the curve  $t \mapsto \mu_t$  such that  $(\mu_t, \mathbf{v}_t)$  satisfies the continuity equation (4.4), where  $\mathbf{v}_t$  is given by

$$\mathbf{v}_t = F(t, \mu_t)$$

for some function  $F$  that satisfies  $F(t, \mu) \in T_\mu \mathbb{W}_2$  for all  $t \in [0, T], \mu \in \mathcal{P}_2(\mathbb{R}^d)$ . Given such a function  $F$  and an initial measure  $\mu_0$ , for discrete times  $t_n = nH$ , we set

$$\mu_{(0)} := \mu_0, \quad \mu_{(n+1)} := (\text{id} + HF(t_n, \mu_{(n)}))_\# \mu_{(n)}. \quad (4.10)$$

so that  $\mu_{(n)} \approx \mu_{t_n}$ .

Observe that (4.7) in Theorem 4.6 says that the local truncation error of Euler's method on the Wasserstein manifold is  $o(H)$ . We now show that, like Euler's method in  $\mathbb{R}^d$ , this method (under stronger assumptions on  $F$ ) has local truncation error  $\mathcal{O}(H^2)$ . We begin this discussion by citing a useful lemma:

**Lemma 4.11** (Proposition 8.1.8 in [2]). *Suppose  $\mu : [0, T] \rightarrow \mathcal{P}_2(\mathbb{R}^d)$  is an absolutely continuous curve satisfying the continuity equation (4.4) with a velocity field  $\mathbf{v}_t$  that satisfies*

$$\int_0^T \int_{\mathbb{R}^d} \|\mathbf{v}_t(x)\| d\mu_t(x) dt < \infty \quad (4.12)$$

and

$$\int_0^T \left( \sup_{x \in B} \|\mathbf{v}_t(x)\| + \text{Lip}(\mathbf{v}_t, B) \right) dt < \infty \quad (4.13)$$

for all compact set  $B \subset \mathbb{R}^d$ . Then for  $\mu_0$ -a.e.  $x \in \mathbb{R}^d$ , the ODE

$$\gamma_x(0) = x, \quad \frac{d}{dt} \gamma_x(t) = \mathbf{v}_t(\gamma_x(t)) \quad (4.14)$$

admits a globally defined solution, and

$$\mu_t = (T_t)_\# \mu_0 \quad \text{for all } t \in [0, T], \quad (4.15)$$

where  $T_t(x) := \gamma_x(t)$ .

Under these (fairly strong) assumptions on the underlying vector field  $\mathbf{v}_t$ , we get a bound on the approximation error that is exactly analogous to the local truncation error of Euler's method for curves with bounded second derivative:

**Theorem 4.16.** *Assume the hypotheses of Lemma 4.11. Fix  $t \in [0, T]$ , let  $H > 0$  such that  $t + H \leq T$ , and let  $\gamma_x : [t, t + H] \rightarrow \mathbb{R}^d$  be the solution to*

$$\gamma_x(t) = x, \quad \gamma'_x(s) := \frac{d}{ds} \gamma_x(s) = \mathbf{v}_s(\gamma_x(s))$$

If  $\gamma_x$  is  $C^2$  for  $\mu_t$ -a.e.  $x \in \mathbb{R}^d$  and

$$\int_{\mathbb{R}^d} \max_{r \in [t, t+H]} \|\gamma''_x(r)\|_2^2 d\mu_t(x) < \infty,$$

then

$$W_2(\mu_{t+H}, (\text{id} + H\mathbf{v}_t)_\# \mu_t) \leq \frac{H^2}{2} \left( \int_{\mathbb{R}^d} \max_{r \in [t, t+H]} \|\gamma''_x(r)\|_2^2 d\mu_t(x) \right)^{1/2}.$$

*Proof.* Define  $T_s : \mathbb{R}^d \rightarrow \mathbb{R}^d$  by  $T_s(x) = \gamma_x(s)$ . By Lemma 4.11,

$$\mu_{t+H} = (T_{t+H})_\# \mu_t,$$

so

$$\begin{aligned} W_2^2(\mu_{t+H}, (\text{id} + H\mathbf{v}_t)_\# \mu_t) &\leq \int_{\mathbb{R}^d} \|T_{t+H}(x) - (\text{id} + H\mathbf{v}_t)(x)\|_2^2 d\mu_t(x) \\ &= \int_{\mathbb{R}^d} \|\gamma_x(t+H) - [x + H\mathbf{v}_t(x)]\|_2^2 d\mu_t(x). \end{aligned}$$

If  $\gamma_x$  is  $C^2$  for a particular  $x \in \mathbb{R}^d$ , then we can write

$$\begin{aligned} \gamma_x(t+H) &= \gamma_x(t) + H\gamma'_x(t) + \int_t^{t+H} \int_t^s \gamma''(r) dr ds \\ &= x + H\mathbf{v}_t(x) + \int_t^{t+H} \int_t^s \gamma''(r) dr ds. \end{aligned}$$

Hence, if  $\gamma_x$  is  $C^2$  for  $\mu_t$ -a.e.  $x \in \mathbb{R}^d$ , then we have

$$\begin{aligned} W_2^2(\mu_{t+H}, (\text{id} + H\mathbf{v}_t)_\# \mu_t) &\leq \int_{\mathbb{R}^d} \left\| \int_t^{t+H} \int_t^s \gamma''_x(r) dr ds \right\|_2^2 d\mu_t(x) \\ &\leq \int_{\mathbb{R}^d} \frac{H^4}{4} \max_{r \in [t, t+H]} \|\gamma''_x(r)\|_2^2 d\mu_t(x). \quad \square \end{aligned}$$

This result says that the local truncation error of Euler's method on the Wasserstein manifold is  $\mathcal{O}(H^2)$ . This suggests that, given some Lipschitz condition on the function  $F$ , the global error should be first order. This is exactly the content of Theorem 4.1, which we can now prove:

*Proof of Theorem 4.1.* We first need to prove that the ODE (4.14) admits a unique solution on  $[0, T]$ . By Lemma 4.11, it suffices to show that  $\mathbf{v}_t := F(t, \mu_t)$  satisfies (4.12) and (4.13). For the first, we have

$$\begin{aligned} \int_0^T \int_{\mathbb{R}^d} \|\mathbf{v}_t(x)\| d\mu_t(x) dt &\leq \int_0^T \int_{\mathbb{R}^d} [\|\mathbf{v}_t(0)\| + \|\mathbf{v}_t(x) - \mathbf{v}_t(0)\|] d\mu_t(x) dt \\ &\leq \int_0^T \int_{\mathbb{R}^d} [\|\mathbf{v}_t(0)\| + L_1 \|x\|] d\mu_t(x) dt \\ &= \int_0^T \|\mathbf{v}_t(0)\| dt + L_1 \int_0^T \int_{\mathbb{R}^d} \|x\| d\mu_t(x) dt. \end{aligned}$$

We assume  $(t, x) \mapsto \mathbf{v}_t(x)$  is  $C^1$ , so

$$\int_0^T \|\mathbf{v}_t(0)\| dt < \infty,$$

and  $t \mapsto \int_{\mathbb{R}^d} \|x\| d\mu_t(x)$  is continuous because  $t \mapsto \mu_t$  is continuous with respect to  $W_2$ , so

$$\int_0^T \int_{\mathbb{R}^d} \|x\| d\mu_t(x) dt < \infty.$$

Hence, we have (4.12). For (4.13), if  $B \subset \mathbb{R}^d$  is compact, then

$$\int_0^T \left( \sup_{x \in B} \|\mathbf{v}_t(x)\| + \text{Lip}(\mathbf{v}_t, B) \right) dt \leq T \left( \sup_{t \in [0, T], x \in B} \|\mathbf{v}_t(x)\| + L_1 \right) < \infty$$

because again  $(t, x) \mapsto \mathbf{v}_t(x)$  is  $C^1$ . Hence, by Lemma 4.11, the ODE (4.14) has a globally defined solution  $\gamma_x$  for  $\mu_0$ -a.e.  $x \in \mathbb{R}^d$ , and since  $(x, t) \mapsto \mathbf{v}_t(x)$  is  $C^1$ , we have that  $\gamma_x$  is  $C^2$  for such  $x$ .

Now, for

$$M = \left( \int_{\mathbb{R}^d} \max_{r \in [0, T]} \|\gamma_x''(r)\|_2^2 d\mu_0(x) \right)^{1/2} < \infty,$$

we will show

$$W_2(\mu_{(n+1)}, \mu_{t_{n+1}}) \leq (1 + H(L_1 + L_2))W_2(\mu_{(n)}, \mu_{t_n}) + \frac{H^2}{2}M. \quad (4.17)$$

By the triangle inequality for  $W_2$ , we have

$$\begin{aligned} W_2(\mu_{(n+1)}, \mu_{t_{n+1}}) &= W_2((\text{id} + HF(t_n, \mu_{(n)}))\# \mu_{(n)}, \mu_{t_{n+1}}) \\ &\leq W_2((\text{id} + HF(t_n, \mu_{(n)}))\# \mu_{(n)}, (\text{id} + HF(t_n, \mu_{t_n}))\# \mu_{(n)}) \quad (*) \\ &\quad + W_2((\text{id} + HF(t_n, \mu_{t_n}))\# \mu_{(n)}, (\text{id} + HF(t_n, \mu_{t_n}))\# \mu_{t_n}) \quad (\dagger) \\ &\quad + W_2((\text{id} + HF(t_n, \mu_{t_n}))\# \mu_{t_n}, \mu_{t_{n+1}}). \quad (\ddagger) \end{aligned}$$

Handling each term separately, we have

$$\begin{aligned} (*) &\leq \|(\text{id} + HF(t_n, \mu_{(n)})) - (\text{id} + HF(t_n, \mu_{t_n}))\|_{L^2(\mu_{(n)})} \\ &= H\|F(t_n, \mu_{(n)}) - F(t_n, \mu_{t_n})\|_{L^2(\mu_{(n)})} \\ &\leq HL_2W_2(\mu_{(n)}, \mu_{t_n}) \end{aligned}$$

$$\begin{aligned} (\dagger) &\leq \|\text{id} + HF(t_n, \mu_{t_n})\|_{\text{Lip}}W_2(\mu_{(n)}, \mu_{t_n}) \\ &\leq (1 + HL_1)W_2(\mu_{(n)}, \mu_{t_n}) \end{aligned}$$

$$(\ddagger) \leq \frac{H^2}{2}M,$$

where we use Theorem 4.16 for the last term.

Given this iterative bound, we recall the analysis of sequences used to derive the global error bound for Euler's method in  $\mathbb{R}^d$ : For a sequence  $\{a_n\}$  with the recursive property that  $a_{n+1} \leq (1 + \alpha)a_n + \beta$  with  $\alpha \neq 0$ , we have

$$a_n \leq e^{n\alpha} \left( a_0 + \frac{\beta}{\alpha} \right) - \frac{\beta}{\alpha}.$$

Applying this to (4.17) with  $\alpha = H(L_1 + L_2)$  and  $\beta = \frac{H^2}{2}M$  gives

$$W_2(\mu_{(n)}, \mu_{t_n}) \leq \frac{HM}{2(L_1 + L_2)} \left( e^{nH(L_1 + L_2)} - 1 \right)$$

as desired. □

Since the global error is proportional to  $H$ , the Wasserstein analog of Euler's method is a first order method for approximating solutions to the continuity equation with prescribed vector field flow.

### 4.3 Euler's Method Using Finite Differences

The above discussion shows that, under strong regularity assumptions on  $F$ , Euler's method on the Wasserstein manifold can approximate solutions to the continuity equation with prescribed vector field flows given by  $F$ . However, as we discussed in Section 3, we rarely have access to the function  $F$  in practice, and so we cannot explicitly compute the velocity field  $\mathbf{v}_t$  to use in Euler's method. Instead, we will only have access to some oracle  $E_h$  that, given a time  $t$  and a measure  $\mu$ , will return an approximation of what that measure would be at time  $t + h$  if allowed to evolve according to  $F$  for some small time step  $h$ . That is, if  $\mu$  is a solution to the continuity equation with  $\mathbf{v}_t = F(t, \mu_t)$ , then the oracle is such that

$$E_h(t, \mu_t) \approx \mu_{t+h}.$$

To perform an Euler-like method, then, we must first approximate the appropriate velocity field, and (4.8) hints that we should approximate it with

$$\mathbf{v}_t^h(x) := \frac{T_{\mu_t}^{E_h(t, \mu_t)}(x) - x}{h} \approx \frac{T_{\mu_t}^{\mu_{t+h}}(x) - x}{h}.$$

Unfortunately, even if  $E_h(\mu_t) = \mu_{t+h}$  exactly, the  $L^2$  convergence in (4.8) is not enough to guarantee that  $\mathbf{v}_t^h(x) \rightarrow \mathbf{v}_t(x)$  pointwise as  $h \rightarrow 0$ . However, the  $L^2$  convergence is still good enough to give a reasonable bound on the local truncation error of using this finite difference approximation in Euler's method:

**Corollary 4.18.** *Suppose  $\mu_t \ll \mathcal{L}^d$  and  $h > 0$ . Set*

$$\mathbf{v}_t^h(x) := \frac{T_{\mu_t}^{E_h(t, \mu_t)}(x) - x}{h}.$$

*Then*

$$W_2(\mu_{t+H}, (\text{id} + H\mathbf{v}_t^h)_\# \mu_t) \leq H \|\mathbf{v}_t - \mathbf{v}_t^h\|_{L^2(\mu_t)} + o(H) \quad (4.19)$$

*as  $H \rightarrow 0$ , and if  $E_h(t, \mu_t) = \mu_{t+h}$ , then  $\|\mathbf{v}_t - \mathbf{v}_t^h\|_{L^2(\mu_t)} \rightarrow 0$  as  $h \rightarrow 0$ .*

*Proof.* First note that (4.8) says that  $\|\mathbf{v}_t - \mathbf{v}_t^h\|_{L^2(\mu_t)} \rightarrow 0$  as  $h \rightarrow 0$  when  $E_h(t, \mu_t) = \mu_{t+h}$ .

For the inequality, by (4.7) we have

$$\begin{aligned} W_2(\mu_{t+H}, (\text{id} + H\mathbf{v}_t^h)_\# \mu_t) &\leq W_2(\mu_{t+H}, (\text{id} + H\mathbf{v}_t)_\# \mu_t) + W_2((\text{id} + H\mathbf{v}_t)_\# \mu_t, (\text{id} + H\mathbf{v}_t^h)_\# \mu_t) \\ &\leq o(H) + \|(\text{id} + H\mathbf{v}_t) - (\text{id} + H\mathbf{v}_t^h)\|_{L^2(\mu_t)} \\ &= o(H) + H \|\mathbf{v}_t - \mathbf{v}_t^h\|_{L^2(\mu_t)}. \quad \square \end{aligned}$$

This is the local truncation error of the Euler-like method

$$\mu_{(0)} = \mu_{t_0}, \quad \mu_{(n+1)} \approx (\text{id} + H\mathbf{v}_t^h)_\# \mu_{(n)}. \quad (4.20)$$

As was alluded to in Section 3, the local truncation error of this method depends on the accuracy of the approximation of the "tangent vector"  $\mathbf{v}_t = F(t, \mu_t)$ .

## 5 Euler-Like Discrete Approximation Algorithm

The above discussion shows that, in the case where the distributions have densities, an Euler-like scheme for approximating future distributions will work as long as the evolution is smooth enough. However, in practical applications, we are often in the setting where we have many discrete particles  $\{x_i(t)\}_{i=1}^N$  evolving in  $\mathbb{R}^d$ . A natural adaptation is to consider the empirical distribution

$$\mu_t^N := \frac{1}{N} \sum_{i=1}^N \delta_{x_i(t)}$$

at time  $t$  and then use the above ideas to describe an Euler scheme for approximating the locations of the particles at discrete times  $t_j$  by approximating  $\mu_{t_j}^N$ . Unfortunately, we are primarily concerned with the setting where the particles themselves do not evolve according to a nice vector field (e.g., they evolve according to some stochastic process), so we cannot directly apply the analysis in Section 4. Instead, we assume that  $\mu_t^N$  is an empirical estimate for some continuous measure  $\mu_t$ , and that the curve  $t \mapsto \mu_t$  is absolutely continuous in the Wasserstein metric so that Theorems 4.2 and 4.6 apply to  $\mu_t$ . In practice, though, we do not have explicit access to the vector field  $\mathbf{v}_t$ . We only have access to the particle locations, and more importantly, we only have access to their locations at discrete times (e.g., at the discrete times of a micro-scale simulation). Thus, to use an Euler-like method, we first must approximate the true velocity field  $\mathbf{v}_t$  with a finite-difference approximation defined at the points in the support of  $\mu_t^N$ : for a small time step  $h$ , set

$$\mathbf{v}_t^{h,N}(x_i(t)) := \frac{T_{\mu_t^N}^{\mu_{t+h}^N}(x_i(t)) - x_i(t)}{h}$$

(where we use Proposition 2.4 to conclude that  $T_{\mu_t^N}^{\mu_{t+h}^N}$  is a well-defined map).

One step of the Euler-like approximation method, then, would be to approximate  $\mu_{t+H}^N$  by

$$\mu_{t+H}^N \approx \tilde{\mu}_{t+H}^N := (\text{id} + H\mathbf{v}_t^{h,N})_{\#} \mu_t^N = \frac{1}{N} \sum_{i=1}^N \delta_{x_i(t) + H\mathbf{v}_t^{h,N}(x_i(t))}. \quad (5.1)$$

**Remark 5.3.** For uniform measures on the same number of points, optimal transport maps are given by permutations of the points in the supports. Formally, there is a permutation  $\sigma \in S_N$  such that

$$T_{\mu_t^N}^{\mu_{t+h}^N}(x_i(t)) = x_{\sigma(i)}(t+h) \quad \text{for all } i \in [N].$$

Thus, in essence, the approximation  $\tilde{\mu}_{t+H}^N$  is computed by allowing the particles to evolve for a short time, relabelling the particles by  $\sigma$ , and then performing an Euler step for each individual particle using the derivative estimate given by the short time step. Figure 5.2 illustrates the approximation scheme in a simple case with 5 particles. The hope is that, up to a (possibly new) relabelling  $\tau$ , we have

$$x_{\tau(i)}(t+H) \approx x_i(t) + H\mathbf{v}_t^{h,N}(x_i(t)) \quad \text{for all } i \in [N],$$

i.e., that  $W_2(\mu_{t+H}^N, \tilde{\mu}_{t+H}^N)$  is small.

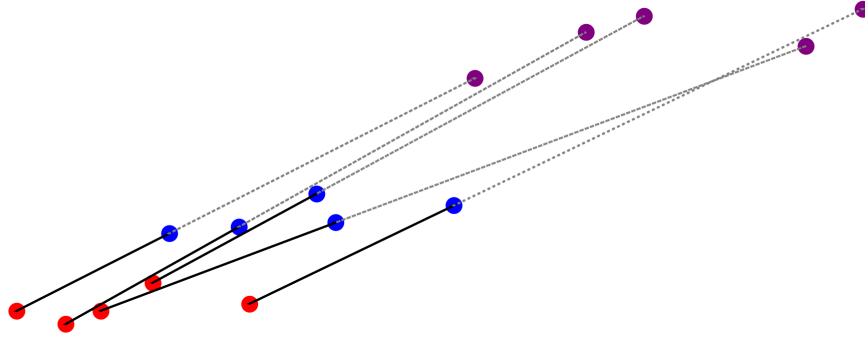


Figure 5.2: Example of LOT Approximation Algorithm applied to a discrete distribution with  $N = 5$  particles.  $\mu_t^N$  is shown in red,  $\mu_{t+h}^N$  in blue, and the OT map  $T_{\mu_t^N}^{\mu_{t+h}^N}$  is shown by the black pairings. We then use (5.1) to compute the approximate distribution  $\tilde{\mu}_{t+H}^N$ , which is shown in purple. The dashed lines demonstrate the relationship between this approximation and an Euler step: the approximation is obtained by taking five Euler-like steps, one for each particle in the distribution, where each particle's velocity corresponds to the optimal transport map from  $\mu_t^N$  to  $\mu_{t+h}^N$ .

**Remark 5.4.** It is important to point out that Corollary 4.18 requires that  $\mu_t$  has density, which is not true in the discrete setting where  $\mu_t^N$  is an empirical measure. A tempting fix is to give each particle a local density, e.g., by setting

$$\hat{\mu}_t := \frac{1}{N} \sum_{i=1}^N \mathcal{N}(x_i(t), \sigma^2 I_d),$$

for some small variance  $\sigma^2$ . This does not resolve the issue, however: if the curves  $t \mapsto x_i(t)$  are not absolutely continuous in  $\mathbb{R}^d$ , then the curve  $t \mapsto \hat{\mu}_t$  is not absolutely continuous on the Wasserstein manifold, so Corollary 4.18 still does not apply. We are often concerned with the case where the particles  $x_i$  are stochastic processes evolving according to some SDE, so the individual particles' curves are nowhere differentiable and hence not absolutely continuous. (This is precisely what we mean by the particles themselves not evolving according to a nice vector field.) Thus, the theoretical transition from the continuous case to the discrete case is not immediately obvious.

We will not fully resolve the theoretical hurdles in this paper, as work into making precise convergence statements in the discrete case is still ongoing. However, we can still give a heuristic argument for why this approximation approach ought to work in the discrete setting as well. The fundamental problem with directly applying Theorem 4.6 to the measures  $\mu_t^N$  is that, in our setting with chaotic individual particles, there is no vector field that describes the evolution of  $\mu_t^N$  on short time scales. However, if we allow the particles to evolve over a sufficiently long time, then there is still a heuristic notion of a direction the particles as a group are traveling. The driving idea is that computing optimal transport maps allows us to access that heuristic.

As an example, consider Figure 5.5. The first image shows 2000 particles evolving according to a standard Gaussian diffusion simulation (described in more detail in Section 6) for a short time, and an arrow drawn between each particle's starting and ending location. The arrows are expectedly chaotic because the particles' motions are individually unpredictable. In contrast, the second image shows an equivalent set of particles diffusing for the same amount of time, except instead of drawing the arrows particle-wise, we compute the optimal transport map from the beginning to the ending

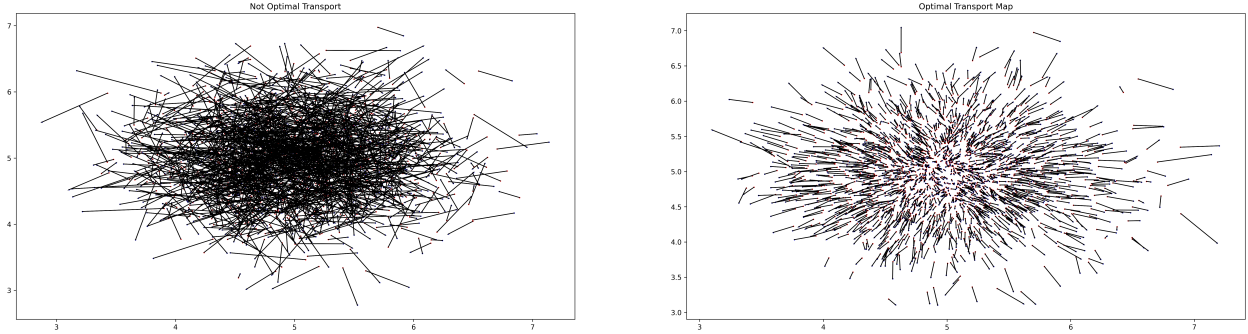


Figure 5.5: Example of the difference between the optimal transport map and the particle-wise map. In the particle-wise image (left), an arrow is drawn to connect each particle’s starting position to its ending position. In the optimal transport image (right), we compute the OT map between the starting and ending distributions and draw an arrow connecting each particle’s starting location to its corresponding output under the OT map. Since the optimal transport map sends each starting particle to the ending particle that it “most likely” corresponds to, the OT map has much more structure. In the OT image, we can clearly see the distribution’s bulk behavior – drifting away from the center in all directions. In the particle-wise image, there is no structure.

distribution. This map reveals an obvious structure in the distribution’s evolution: the distribution is slowly drifting away from the center in all directions, exactly the expected behavior of a Gaussian distribution diffusing over time. Even though the actual time derivatives are meaningless because Brownian motion is not differentiable, these finite differences over a slightly longer time step indeed give a reasonable approximation of the vector field that describes the distribution’s evolution.

## 5.1 Choosing an Appropriate Step Size

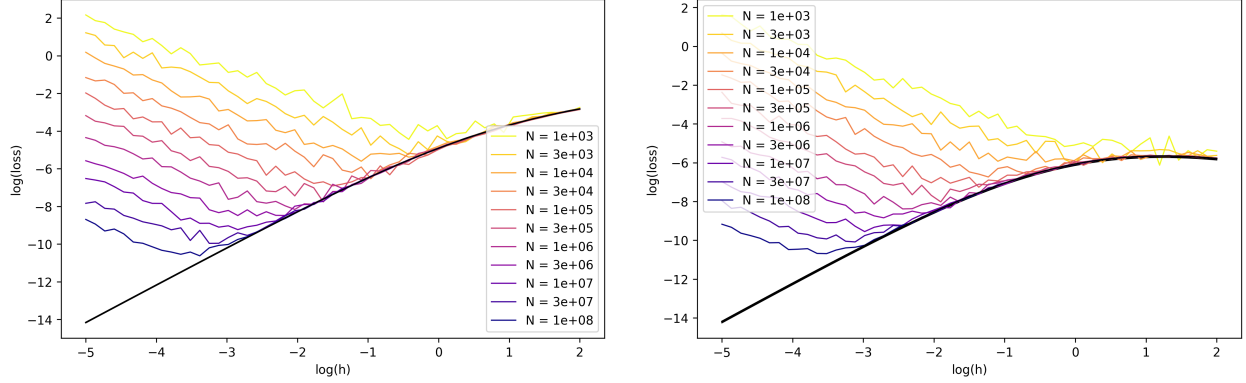
The quality of the approximated distribution clearly depends on how well this discrete vector field captures the evolution of the overall distribution. In the continuous case, equation (4.8) says that the error in the vector field approximation, given by  $\|\mathbf{v}_t - \mathbf{v}_t^h\|_{L^p(\mu_t)}$ , decreases as  $h$  decreases. This is a standard phenomenon in numerical approximations: the smaller the time step, the better the approximation.

In the discrete case, however, the fact that the particle-wise finite differences give a terrible approximation of the vector field (as seen in the first image in Figure 5.5) means there is a competing desire to keep  $h$  sufficiently large in practice. More specifically, each  $x_i(t)$  is a continuous curve in  $t$ , so choosing  $h$  small enough will make  $T_{\mu_i^N}^{\mu_i^N+h}(x_i(t)) = x_i(t+h)$ , and then the vector field approximation produced by the optimal transport map really is just a particle-wise finite difference approximation of each particle’s velocity. We know that this particle-wise construction does not accurately depict the overall flow of the distribution, so choosing  $h$  too small results in a bad approximation of the vector field.

We can empirically verify this phenomenon by estimating  $\|\mathbf{v}_t - \mathbf{v}_t^h\|_{L^p(\mu_t)}$  in cases where  $\mathbf{v}_t$  is theoretically known, e.g., Gaussian diffusion. For standard Gaussian diffusion described by the SDE

$$dX_t = dW_t, \quad X_0 = 0,$$

the solution is  $X_t \sim \mu_t := \mathcal{N}(m = 0, \sigma = \sqrt{t})$ .



(a) True approximation error: the black curve is the log of theoretical finite difference error  $\|\mathbf{v}_t - \mathbf{v}_t^h\|^2$  versus the log of the step size  $h$ . The colored curves are the log of the discrete approximation error  $\|\mathbf{v}_t - \mathbf{v}_t^{h,N}\|^2$  for various values of  $N$ .

(b) Estimated approximation error: the black curve is the log of theoretical finite difference error  $\|\mathbf{v}_t^h - \mathbf{v}_t^{2h}\|^2$  versus the log of the step size  $h$ . The colored curves are the log of the discrete approximation error  $\|\mathbf{v}_t^{h,N} - \mathbf{v}_t^{2h,N}\|^2$  for various values of  $N$ .

Figure 5.6: Results of vector field error computations for Gaussian diffusion in one dimension, and comparison with an estimated error using the difference between consecutive approximations.

Moreover, since optimal transport maps between Gaussians has a closed form expression, we can explicitly compute the vector field to be

$$\mathbf{v}_t(x) = \frac{x}{2t}.$$

By knowing the true vector field  $\mathbf{v}_t$ , we can experimentally estimate the error in the discrete approximation  $\mathbf{v}_t^{h,N}$  by computing  $\|\mathbf{v}_t - \mathbf{v}_t^{h,N}\|_{L^2(\mu_t^N)}$ . To isolate the effects of the discrete approximation (as opposed to the error caused by the finite difference estimate), we compute the finite difference vector field

$$\mathbf{v}_t^h(x) = \frac{T_{\mu_t}^{\mu_{t+h}}(x) - x}{h} = \frac{x(\sqrt{\frac{t+h}{t}} - 1)}{h}$$

and then compute the expected error in the finite difference approximation  $\|\mathbf{v}_t - \mathbf{v}_t^h\|_{L^2(\mu_t^N)}$ .

We perform this experiment for different values of  $h, N$ , and the plots are shown in Figure 5.6a. We notice that for each value of  $N$ , there is an approximately optimal value of  $h$  that minimizes the approximation error, and that this optimal value of  $h$  decreases as  $N$  increases. We also see that, for very small values of  $h$ , the error is very large (which is expected from the discussion above), and that for larger values of  $h$ , the discrete approximation is about as good as the true finite difference approximation. This indicates that, indeed, as the step size increases, the optimal transport map better captures the distribution's bulk behavior, and the limiting factor on choosing  $h$  too big is the fact that we are approximating a derivative using a finite difference. While these experimental results do not precisely explain how to formalize this behavior, they do corroborate our discussion that there is an optimal value of  $h$  that decreases as the number of samples increases.

We expect that this phenomenon appears in most random particle systems one would be interested in studying using optimal transport. Unfortunately, even this empirical analysis is not possible unless the theoretical vector field  $\mathbf{v}_t$  is known *a priori*. In practice, we never have access to this vector field, and so we need a way to determine the optimal  $h$  without relying on comparing the

approximated vector field to the true one. Instead, we perform another experiment to assess the viability of a simple intrinsic metric: how much the approximation of the vector field changes after another short step. That is, we compute the observed difference in approximated vector fields  $\|\mathbf{v}_t^{h,N} - \mathbf{v}_t^{2h,N}\|_{L^2(\mu_t^N)}$  and compare with the expected difference between two consecutive finite difference approximations  $\|\mathbf{v}_t^h - \mathbf{v}_t^{2h}\|_{L^2(\mu_t^N)}$ . The results are shown in Figure 5.6b. While the correspondence is not perfect, the plots are remarkably similar, which indicates that this heuristic is a reasonable substitute for the true error computation performed above. Once again, without knowledge of the underlying true vector field, it is difficult to perform more experiments to investigate this relationship. Investigating whether this correspondence holds in settings more general than Gaussian diffusion is an ongoing area of study.

## 5.2 Statistical Averaging

When dealing with random particle systems, it is helpful to gather many vector field approximations and compute an average. There are many possible approaches to achieve this, but perhaps the simplest is to take an average of finite differences computed with a range of different time steps over some interval. If we consider the middle of this interval to be the time at which we are hoping to approximate the derivative, then taking an average of both forwards and backwards differences becomes equivalent to taking an average of centered differences. Explicitly, for a fixed time step  $h$  and discrete times  $t_0 - kh =: t_{-k}, \dots, t_0, \dots, t_k := t_0 + kh$ , we set

$$\begin{aligned} \mathbf{v}_{t_0}^{h,k,N}(x_i(t_0)) &:= \frac{1}{2k} \sum_{\substack{j=-k \\ j \neq 0}}^k \mathbf{v}_t^{jh}(x_i(t_0)) \\ &= \frac{1}{2k} \sum_{\substack{j=-k \\ j \neq 0}}^k \frac{T_{\mu_{t_0}^N}^{\mu_{t_0}^N}(x_i(t_0)) - x_i(t_0)}{jh} \\ &= \frac{1}{k} \sum_{j=1}^k \frac{T_{\mu_{t_0}^N}^{\mu_{t_0}^N}(x_i(t_0)) - T_{\mu_{t_0}^N}^{\mu_{t_0}^N-j}(x_i(t_0))}{2jh}. \end{aligned}$$

Note that the last line is the average of  $k$  centered-difference approximations of  $\frac{d}{ds} T_{\mu_t^N}^{\mu_{t+s}^N}(x_i(t))$  centered at  $t_0$  and with time steps  $h, 2h, \dots, kh$ . This is the method we use in practice.

This method for approximating the derivative works well on toy examples where the vector field is explicitly calculable in theory (e.g., diffusion), and the associated approximation scheme described by (5.1) gives reasonable predictions for the overall distribution. As we will see in Sections 6 and 7,

$$\mu_{t+H}^N \approx \tilde{\mu}_{t+H}^N := (\text{id} + H \mathbf{v}_t^{h,k,N})_{\#} \mu_t^N$$

gives a reasonable approximation for the actual distribution  $\mu_{t+H}^N$  in some standard particle system examples.

### 5.3 Euler-Like Approximation Method

In order to approximate the particle distribution over a long time, we need to perform many of these Euler-like steps. Since each one requires a finite difference approximation of a vector field, we need a way to allow the distribution to continue evolving “naturally” after taking each Euler-step forward. This may be impossible if the particles are some physical objects, but it is trivial if we suppose the “true” evolution of the particles is given by some micro-scale model. With a micro-scale simulation, we can simply re-initialize the positions of the particles to be those of  $\tilde{\mu}_{t_0+H}^N$  and start the simulation again, gather new derivative estimates, and then step forward again to approximate  $\tilde{\mu}_{t_0+2H}^N$ . For this reason, we henceforth only consider particle systems for which we have a known micro-scale model, and we consider the result of running the micro-scale simulation as the true curve  $(\mu_t^N)_{t \geq 0}$ .

One potential hurdle with the approach of taking multiple steps and re-initializing particle locations after each, however, is that the approximated distribution will be slightly different than the true distribution, and running the micro-scale simulation on the approximated distribution might result in behavior that is initially dominated by the approximated distribution returning to a relative equilibrium. To account for this, and to make sure the approximated derivatives are capturing mostly the long-term dynamics, we must allow the approximated distribution to evolve according to the micro-scale simulation for a prescribed “burn-in” time  $H_R$  before starting to take samples to use in the computation of  $\mathbf{v}_{t_0+H+H_R}$ . This ensures that any fringe effects from the approximation step are washed away before we start approximating the flow vector field describing the distribution’s evolution.

**Remark 5.7.** This “burn-in” period also has the added benefit of avoiding pathologies that can arise from using Euler’s method on, e.g., Wasserstein gradient flows [33]. For example, there is no guarantee that the map  $x \mapsto x + H\mathbf{v}_t(x)$  is injective, and in particular this means that the approximated distribution  $\tilde{\mu}_{t+H}$  may not have a density. In the discrete setting, this means there may be locations with a high density of approximated particles (or even particles with exactly the same approximated location), which could result in irregularities in the computed velocity field. By allowing the particle system to “burn in” after each approximating step, we ensure that the particles’ density is roughly smooth. For an illustration of how the “burn-in” time allows the density to smooth, see Figures 6.3 and 6.4. Empirical tests indicate that this “burn-in” is essential for this method to work well, and understanding these benefits theoretically is a subject of ongoing work.

Putting everything together, the overall method for approximating the distribution  $\mu_T^N$  for large  $T$  is as follows. We fix values for the parameters

$h$	the time of one step of the micro-scale simulation
$k$	the number of centered differences to average
$H_S := kh$	half the length of the derivative-sample time window
$H$	the length of each approximating step
$H_R$	the burn-in time after each approximating step
$\Delta := H_S + H + H_R$	the time difference between approximations

and then do

1. Run the micro-scale simulation for some start-up time  $S$  (by taking  $S/h$  micro-scale steps) to allow the initial distribution  $\mu_{t_0}$  to reach a relative equilibrium (if necessary). Call the initial distribution  $\mu_{(-1)+H_R}$ .
2. For each approximating step  $n = 0, \dots, N_T$ :
  - (a) Set  $\mu_{(n)-kh} := \mu_{(n-1)+H_R}$ , and take  $2k + 1$  micro-scale steps to get distributions

$$\mu_{(n)-kh}^N, \dots, \mu_{(n)}^N, \dots, \mu_{(n)+kh}^N.$$

- (b) For each  $x_i$  in the distribution  $\mu_{(n)}^N$ , compute

$$\mathbf{v}_{(n)}^{h,k,N}(x_i) = \frac{1}{k} \sum_{j=1}^k \frac{T^{\mu_{(n)}^N + jh}(x_i) - T^{\mu_{(n)}^N - jh}(x_i)}{2jh}$$

- (c) Set

$$\mu_{(n)+H}^N := (\text{id} + \mathbf{v}_{(n)}^{h,k,N}) \# \mu_{(n)}^N.$$

- (d) Take  $\frac{H_R}{k}$  micro-scale steps to allow the distribution burn-in. Call the resulting distribution  $\mu_{(n)+H_R}^N$

3. Run the micro-scale simulation for some final recover time  $R$  (by taking  $R/h$  micro-scale steps) to ensure any fringe errors in the approximations are minimized (e.g., that the distribution has indeed reached a true steady state).

For discrete times  $t_n := n(H_S + H + H_R)$ , this method approximates  $\mu_t^N \approx \mu_{(n-1)+H_R}^N = \mu_{(n)-kh}^N$ . We also have  $\mu_{(n)}^N \approx \mu_{t_n+kh}$ , and similarly for all empirical distributions obtained at different steps. We can also say that  $\mu_{(n)+H}^N \approx \mu_{t_n+kh+H}$ , but this approximation is likely less good because the distribution has not had time to burn-in yet.

**Remark 5.8.** The above scheme reduces the number of micro-scale steps required to reach the desired end time (as compared to equivalent simulations that only use micro-scale steps) by a factor of  $\frac{H_S+H_R}{H_S+H_R+H}$ , so ideally we would like to have  $H \gg H_S + H_R$  so that the speed-up is nontrivial. Experiments on some toy examples (Sections 6 and 7) demonstrate that, with well-chosen values, the above scheme works well to predict long-term behavior of distributions while also giving meaningful speed-up.

**Remark 5.9.** Another hurdle with this scheme is that it only gives a way to approximate future *locations* of particles. This means that, strictly speaking, this scheme only works for particle clouds that evolve according to position-dependent micro-scale simulations, for example, Euler-Maruyama models of the form

$$X_{t+h} = X_t + \mu(X_t)h + \sigma(X_t)Z_t$$

where  $Z_t \sim \mathcal{N}(0, h)$ . Since micro-scale models of this form are time-independent, nothing needs to be updated between predicting steps, i.e., between steps 2(a) and 2(d) of the above algorithm. However, if the micro-scale model depends on anything other than the position of the particle, then this data must also be predicted across the predicting step taken in step 2(c) above. In general,

there is no particular method for doing this, but we will discuss ad hoc approaches as they come up in Section 7.

## 6 Experiments with Gaussian Diffusion Particle Systems

For particle systems in one dimension, computing the optimal transport map amounts to sorting the particle locations. While similar work with sorting particles has been explored before (e.g., [29]), one of the advantages to framing this approximation algorithm in the context of optimal transport is that it easily generalizes to higher dimensions. In fact, Corollary 4.18 does not depend on the ambient dimension (although it is reasonable to expect that the constants in the convergence rate depend on the dimension). To empirically verify the claim that this approximation scheme is effective in higher dimensions, we compare the approximations with an actual numerical simulation of Gaussian diffusion in two dimensions.<sup>1</sup> We model standard Brownian motion by the Euler-Maruyama numerical scheme

$$x_i(t_{j+1}) := x_i(t_j) + v_c \cdot Z_i(t_j), \quad x_i(0) = x_i$$

where  $Z_i(t_j) \sim \mathcal{N}(0, hI_2)$  are i.i.d. and  $t_j = hj$  for some small time step  $h$ . If we consider  $\{x_i(0)\}_{i=1}^N$  to be  $N$  independent samples from an initial distribution  $\mu_0$ , then the empirical distributions

$$\mu_{t_j}^N := \frac{1}{N} \sum_{i=1}^N \delta_{x_i(t_j)}$$

give an empirical estimate of the distribution  $\mu_{t_j}$ , where  $\mu_{t_j}$  is the law of the solution to the SDE

$$dX_t = v_c \cdot dW_t, \quad X_0 \sim \mu_0.$$

at time  $t_j = jh$ . To ensure that this system approaches a steady-state that has positive density, we consider the case of Brownian motion in a bounded domain  $[x_{min}, x_{max}] \times [x_{min}, x_{max}]$ . To achieve this numerically, we add the condition that if  $x_i(t+h)$  is outside the allowed domain, then we reflect it across the nearest boundary (and repeat if necessary). The steady-state distribution is then the uniform distribution on  $[x_{min}, x_{max}] \times [x_{min}, x_{max}]$ .

Before we run the approximation scheme, we first run the above diffusion micro-scale simulation from  $t = 0$  to  $t = T$  with the parameters shown in Table 6.1. Figure 6.2 shows scatter plots of the particles over time. We consider this data to be the “control” data, and we will compare the results of our approximation algorithm against these control distributions.

We then run the approximation algorithm with the same parameters as above (Table 6.1) and the

---

<sup>1</sup>Simulation of Gaussian diffusion is computationally cheap, so there is little benefit to using our Euler-like approximation algorithm. However, Gaussian diffusion resembles more computationally expensive models in a few key ways, so it is a useful toy model to ensure our algorithm performs reasonably in a standard setting. For an example of a more expensive micro-scale simulation where our algorithm does indeed provide nontrivial computational speed-ups, see Section 7.

$N = 10,000$	number of independent particles
$h = 1/16$	micro-scale simulation step size
$v_c = 1/8$	particle “speed”
$x_i(0) = (5, 5) \quad \forall i \in [N]$	initial particle locations
$[x_{min}, x_{max}] \times [x_{min}, x_{max}] = [0, 10] \times [0, 10]$	domain bounds
$T = 2000$	end time

Table 6.1: Parameters for 2-D diffusion micro-scale simulation.

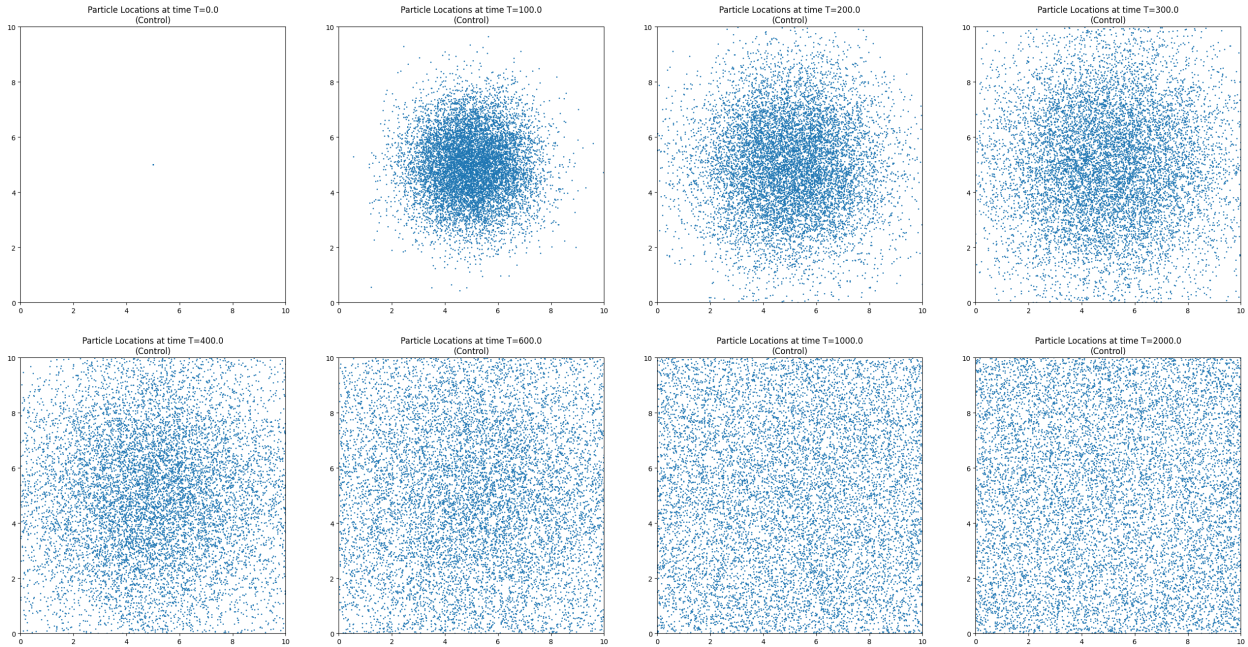


Figure 6.2: Scatter plots of particle locations at equally spaced times  $t$  from  $t = 0$  to  $t = 2000$  for the control simulation of 2-D Gaussian diffusion. We allow the Euler-Maruyama micro-scale simulation (with the parameters described in Table 6.1) to run until  $t = 2000$ , which empirically is long enough for the distribution to reach steady state.

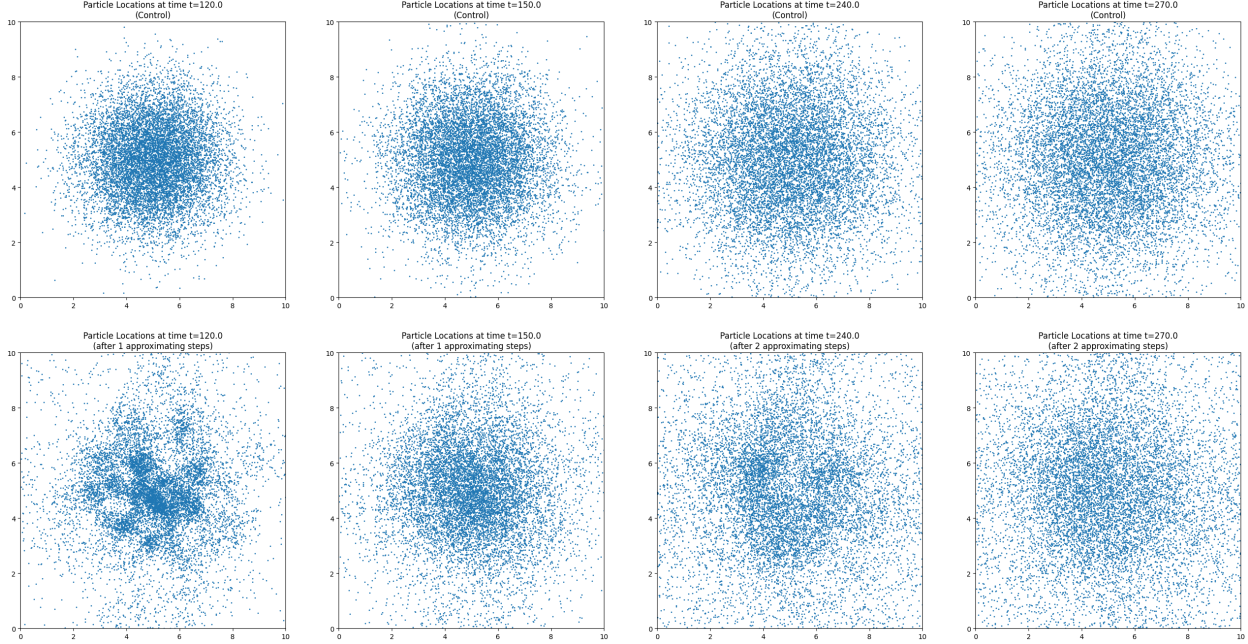


Figure 6.3: Scatter plots of particle locations after the first two approximating steps (bottom) compared with corresponding times from the control simulation (top). We run the micro-scale simulation until  $t = 30$  (not pictured), approximate to  $t = 120$  (left-most), recover until  $t = 150$  (second from left), then approximate to  $t = 240$  (second from right), and recover until  $t = 270$  (right-most).

following additional parameters (as defined in Section 5):

$S = 30$	length of start-up time
$k = 80$	number of centered differences to average
$H = 85$	length of each big approximating step
$H_R = 30$	recovery time after each approximating step
$N_T = 16$	number of approximating steps
$R = 50$	length of additional recover time after last approximating step.

Note that the total length of this simulation, then, is

$$T = S + N_T(H_S + H + H_R) + R = 30 + 16(5 + 85 + 30) + 50 = 2000.$$

Figure 6.3 shows the distributions obtained after the first two approximating steps ( $t = 120, 240$ ), the distributions after the  $H_R = 30$ s recovery time ( $t = 150, 270$ ), and the distributions from the control simulation at the corresponding times for comparison. Similarly, Figure 6.4 shows the last two approximating steps ( $t = 1800, 1920$ ) and corresponding recovery times ( $t = 1830, 2000$  — recall that the last recovery time has an additional  $R = 50$ s). In both figures, we notice that the distributions immediately after the approximating steps look very different than the control distributions at the corresponding time — the density of points is not as smooth as it should be. This is exactly why the recovery time is critical: if we started approximating derivatives immediately

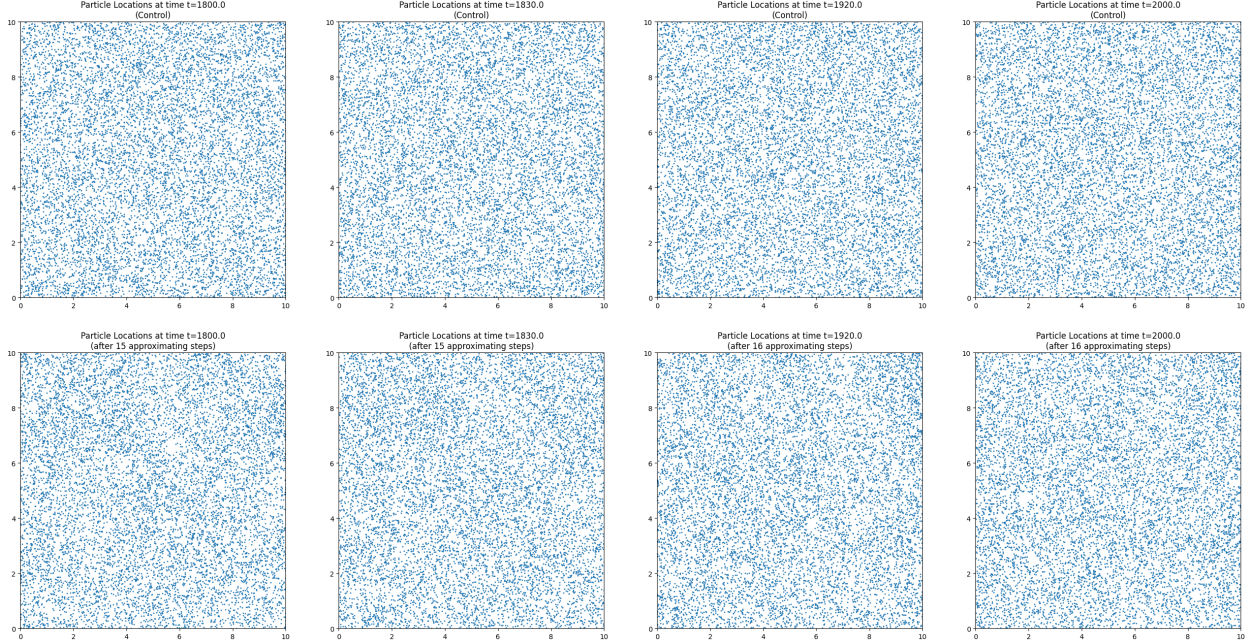


Figure 6.4: Scatter plots of particle locations after the final two approximating steps (bottom) compared with corresponding times from the control simulation (top). We use data near  $t = 1710$  (not pictured) to approximate to  $t = 1800$  (left-most), recover until  $t = 1830$  (second from left), then approximate to  $t = 1920$  (second from right), and finally recover until  $t = 2000$  (right-most), the end time.

after the approximating step, the short-term behavior would be dominated by the distribution returning to a smooth Gaussian, and the longer-term diffusion behavior would be masked.

Looking at Figure 6.3, we can see that 30 seconds of “burn-in” seems to be long enough for the distribution to qualitatively return to a roughly smooth Gaussian. This corresponds to the distribution having “recovered” as much as possible and reached a relative equilibrium, at which point the long-term dynamics are once again dominating the behavior of the distribution. Accurately determining when this occurs is critical to selecting an optimal value for the duration of this recovery window. Our current approach is to pick this value based on observed experimental data, but one could devise other algorithms that adaptively determine the recovery time.

To assess the accuracy of the approximations, we can compute the  $W_2$  distance between the control distribution  $\mu_t^N$  and the approximated distribution  $\tilde{\mu}_t^N$  at all times  $t$ . A plot of  $W_2(\mu_t^N, \tilde{\mu}_t^N)$  versus time is shown in Figure 6.5. Based on this plot, as well as the scatter plots comparing the approximations to the control distributions, we conclude that the approximation algorithm does a good job of predicting the evolution of the particle system.

## 6.1 Computational Advantage

Overall, with the parameters described above, the algorithm only requires 1/3 as many micro-scale steps as the control simulation (10 seconds of derivative-approximation and 30 seconds of recovery for every 120 seconds of simulated time). A natural question is whether we can achieve a better ratio while retaining the accuracy in approximations. The three ways to do this would be to decrease

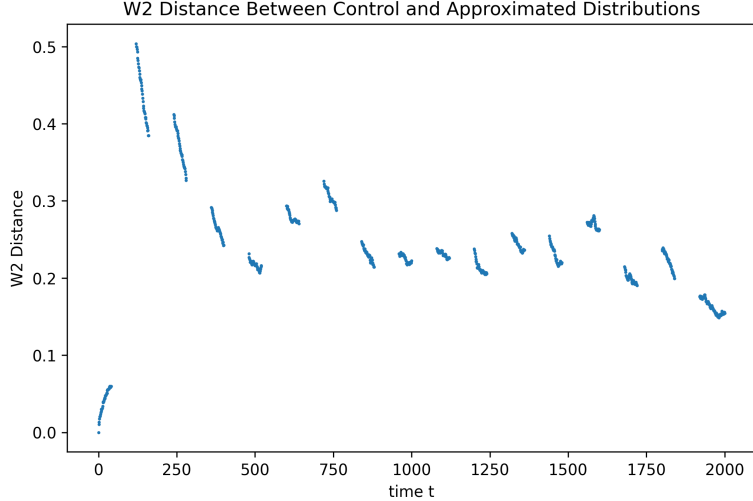


Figure 6.5: We compute  $W_2(\mu_t^N, \tilde{\mu}_t^N)$ , the 2-Wasserstein distance between the control distribution  $\mu_t^N$  and the approximate distribution  $\tilde{\mu}_t^N$ , as a form of “approximation error.” We plot these values at all times  $t$  for which an approximate distribution exists (recall that the point of the approximation algorithm is that we can skip forward in time, so not all times have corresponding approximate distributions). We notice that the approximation error quickly decreases at the start of most recovery periods, and that the approximations stop improving accuracy after about 1000s. Since the control distributions have reached steady state by then, we conclude that the approximations have reached a rough steady state as well.

the recovery time  $H_R$ , to decrease the derivative-approximation window  $H_S$ , or to increase the approximation step size  $H$ . We will address each of these separately.

The length of the “burn-in” period needs to be long enough for the distribution to reach relative equilibrium, and in this case, this duration is a function of how smooth the distributions are after each approximating step. The first approximation in Figure 6.3 shows that the approximated distributions can have particles clumped together in irregular ways. One way to reduce this behavior may be to attempt to smooth the approximated vector field  $\mathbf{v}_t^{h,N}$ , e.g., using a kernel smoothing technique. With the current setup and parameters, however, experimental evidence suggests that a burn-in time of  $H_R = 30$  seconds is approximately optimal.

Decreasing the derivative window  $H_S$  has a similar story. We have observed that the approximation accuracy also noticeably decreases with any substantial decrease in  $H_S$ . It is also important to point out that  $H_S$  is considerably smaller than  $H_R$ , so even decreasing  $H_S$  to 0 while keeping  $H_R$  fixed would only improve the micro-step ratio to  $1/4$ . The biggest improvements will come from decreasing  $H_R$  or increasing  $H$ .

The last way to achieve a better speed-up ratio is to take larger approximating steps by increasing  $H$ . Any discussion about how far we can reasonably step and still get an accurate approximation quickly becomes a discussion about the appropriate notion of a second derivative, which is discussed in detail in Section 4. However, we can get a good visual understanding of whether the system is evolving linearly by doing a dimension-reduction on the OT maps. By fixing a common (discrete) reference measure  $\sigma$ , we can compute the optimal transport maps  $T_\sigma^{\mu_t^N}$  and  $T_\sigma^{\tilde{\mu}_t^N}$ . This gives a universal embedding which we can then use to perform PCA. Explicitly, we can vectorize the map

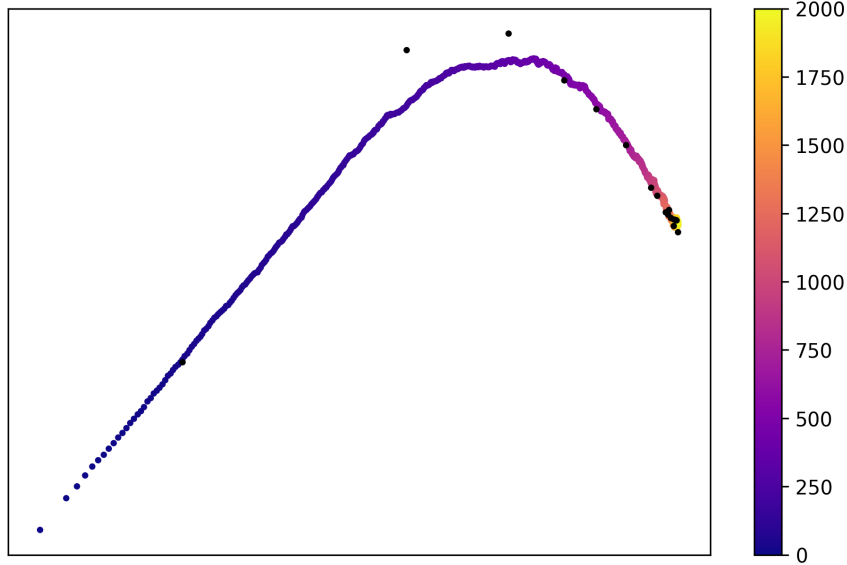


Figure 6.6: Projections of distributions onto the two principal components of the control distribution’s evolution over time. The solid rainbow curve shows the control distribution, where the color represents time according to the color bar at the right. The black dots represent the approximated distribution (after the burn-in period). We see that the approximated distribution closely tracks the control distribution.

$T_{\sigma}^{\tilde{\mu}_t^N}$  so that the map

$$\mu \mapsto T_{\sigma}^{\mu}$$

gives an embedding of distributions into a high dimensional  $\mathbb{R}^{N \times d}$ , where  $N$  is the number of particles in  $\sigma$  (10,000 in our case) and  $d$  is the ambient dimension (here  $d = 2$ ).

We can then perform a PCA to reduce the dimension of this embedding, and this is shown in 6.6. This image gives a good heuristic argument that the distribution is indeed evolving “linearly” in the sense that the OT maps are following a trajectory that appears to have small second derivative at most times. Of course, data is lost in the dimension reduction, but the global evolution of the distribution appears to be roughly smooth. Moreover, the plot indicates that the  $H = 85$  approximating step size is small enough that it places the approximated distribution near the control curve, but it also indicates that stepping much farther in that direction would quickly lead to the approximations being considerably farther from the control curve, especially for the first few approximating steps. Later steps could be longer since the distribution is close to the steady state, and hence the derivative of the optimal transport maps is very small. With small derivative, even large steps would not result in a large change. However, if we require a fixed approximating time for all steps, then  $H = 85$  is approximately optimal. As discussed in Section 4, specifically Theorem 4.16, the optimal step size  $H$  should be a function of the “second derivative” of the curve, so a direction for future work is to attempt to dynamically adjust the length of this step based on an appropriate estimate of the second derivative.

## 6.2 Comparison with Particle-wise Approach

To see the benefit of using optimal transport, we compare the above experiments to the equivalent experiments without using OT, i.e., by keeping track of individual particles, attempting to approximate their derivative, and then taking an Euler step in that direction. Explicitly, instead of approximating  $\mathbf{v}_{t_0}(x_i(t_0))$  by using

$$\mathbf{v}_{t_0}(x_i(t_0)) \approx \frac{1}{k} \sum_{j=1}^k \frac{T_{\mu_{t_0}^N}^{\mu_{t_0}^N}(x_i(t_0)) - T_{\mu_{t_0}^N}^{\mu_{t_0}^N}(x_i(t_0))}{2jh},$$

we could instead attempt to approximate  $\mathbf{v}_{t_0}(x_i(t_0))$  simply by computing

$$\frac{1}{k} \sum_{j=1}^k \frac{x_i(t_0 + jh) - x_i(t_0 - jh)}{2jh},$$

effectively attempting to approximate  $x_i'(t_0)$  (ignoring the fact that this derivative does not actually exist for particles evolving according to Brownian motion). This approach is extremely similar to the optimal transport approach, except we do not relabel any of the particles. As described in Remark 5.3, we can think of the optimal transport map as relabelling each particle in the target distribution based on which particle in the reference distribution most likely moved to become that particle, but if we ignore the relabelling process, we simply get an approximation for the velocity of each individual particle. Intuitively, this should give a much worse understanding of how the overall distribution is evolving, and indeed this is exactly what the experiments show.

We perform exactly the same experiment with the same parameters as above, with the only change being how we compute the velocity field  $\mathbf{v}_t^{h,k}$ . Figure 6.9 shows the result of the first two approximating steps using the particle-wise approach to compute  $\mathbf{v}_t^{h,k}$ . We see that the approximated distribution immediately becomes uniform and does not match the corresponding control distribution at all. This shows that the optimal transport maps are an essential component of this prediction algorithm.

**Remark 6.7.** In the case where  $x_i(t)$  is differentiable for all  $t$ , we can interpret

$$\frac{1}{k} \sum_{j=1}^k \frac{x_i(t_0 + jh) - x_i(t_0 - jh)}{2jh}$$

as approximating  $x_i'(t)$ . In order for this to give an accurate approximation, we need  $x_i'(t)$  to be an accurate approximation of  $\mathbf{v}_t(x_i(t))$ , which may yet hold under some conditions. In particular, this approximation becomes better as each particle's behavior becomes more deterministic. Thus, the more chaotic each particle's motion is on short time scales, the greater the advantage is to using optimal transport over making predictions particle-wise.

**Remark 6.8.** In the case of diffusion, it is easy to understand why the particle-wise estimate of the vector field does not capture the correct bulk behavior at all. For any individual particle, its average velocity from  $t$  to  $t + h$  is a normal random variable with mean 0 because it is simulating a standard Brownian motion. In particular, the estimate for its velocity vector is independent of its

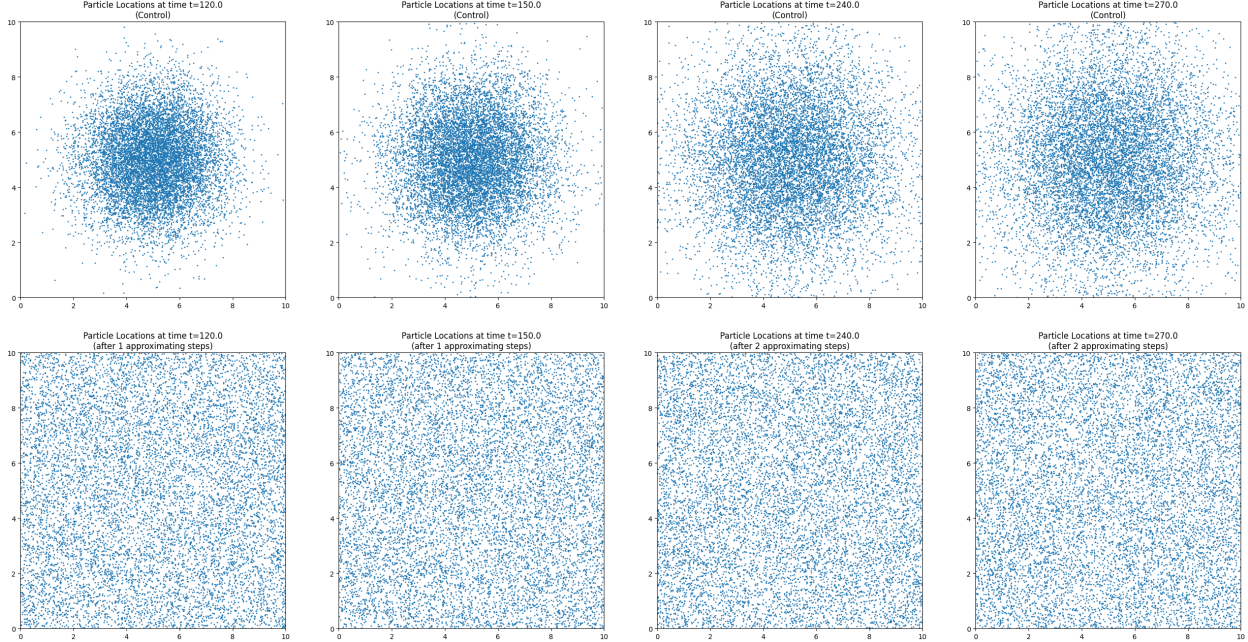


Figure 6.9: Scatter plots of particle locations after the first two approximating steps (bottom) compared with corresponding times from the control simulation (top). The only difference in the approximation algorithm is that we do not compute an optimal transport map. Instead, we compute each individual particle’s average velocity (similar to Figure 5.5). We see that we immediately lose all structure in the approximate distribution because an individual particle’s velocity is unpredictable (in particular, it is independent of position).

current position, which means there will be no structure to the vector field created by computing particle-wise velocities. However, we know analytically that the bulk distribution evolves according to a nonzero vector field — the distribution slowly spreads out over time. This spreading-out movement is the evolution that we want the vector field to pick out, and indeed it is the structure that the optimal transport map captures (see Figure 5.5), but it is completely unrelated to the expected motion of the individual particles.

## 7 Chemotactic Mobility of Bacteria

### 7.1 Problem Setup

The diffusion experiments described in Section 6 have a simple property where the micro-scale simulation only depends on the locations of the particles. This time independence allows us to approximate large-time steps within reasonable error bounds. However, some micro-scale models, such as bacterial locomotion by chemoattractant, are intertwined with other spatiotemporal variables, like a chemoattractant profile. As a result, a proper re-initialization of the micro-scale properties at the predicted location is required for an approximation of a large-time step of all dependent variables, leading to a challenging problem.

In order to demonstrate the effectiveness of the suggested approximation algorithm in a complex micro-scale simulation, we have applied the method to a biological application — the chemotactic movement of bacteria. The mobility of bacteria is affected by the presence of chemoattractant

(specifically, its spatial derivative). However, when we approximate the location of bacteria after a large time step, we may lose the actual trajectory of the bacteria due to a lack of information about the chemotactic effect, resulting in inaccurate predictions. If the chemoattractant profile is smooth enough in space, the microscopic properties of bacteria can be re-initialized within a short recovery time and then follow slow dynamics.

The chemotactic mobility of bacteria has been simulated using a microscopic and stochastic simulator [29, 19]. In this paper, we provide a brief description of variables and a summary of the setup for this micro-simulator. For more theoretical and technical details, please refer to the cited papers.

Here are brief descriptions of the variables in the micro-simulator we discussed in this paper as follows:

- $N$ : the number of bacteria (the number of simulations).
- $x \in \mathbb{R}^d$ :  $d$ -dimensional position vector for each bacteria.
- $s^{(i)} \in \{0, 1\}$ , ( $i = 1, \dots, 6$ ): indicator of rotating direction of flagella,  $s^{(i)} = 0$  clockwise or  $s^{(i)} = 1$  counterclockwise. If more than three flagella are rotating counterclockwise, bacteria start moving.
- $h$ : microscopic time step
- $v_{\text{cell}}$ : the swimming speed of each bacteria
- $S(x)$ : chemoattractant profile

For reference (ground truth), we run the simulation without prediction to establish a “control” as the ground truth behavior of the system. We use the same parameters as in [29, 19] with only the following changes:

$N = 10,000$	number of bacteria
$h = 1/16$	microscopic time step
$v_{\text{cell}} = 0.003$ (= 30 $\mu\text{m/s}$ )	swimming speed of bacteria
$S(x) = \text{NormPDF}(\mu = 6.5, \sigma = 1.35)$	chemoattractant profile

Histograms of bacteria positions at different times in the control simulation are shown in Figure 7.1.

To simulate the next time step, the micro-scale simulator requires not only current bacteria locations but also all microscopic quantities. However, the suggested algorithm described in Section 5 predicts only the *locations* of bacteria after the next approximating step, resulting in a lack (or missing) of microscopic quantities. Hence, after the approximating time step, the suggested algorithm requires the re-initialization step of microscopic quantities, such as  $u_1, u_2$ , and  $s^{(i)}$ . Even though some (quantitatively not but) qualitatively good re-initializations quickly reach slow dynamics, we suggest a better re-initialization scheme based on the history of microscopic quantities and demonstrate a more accurate prediction of bacteria density distribution over multiple approximation steps, see the following sections.

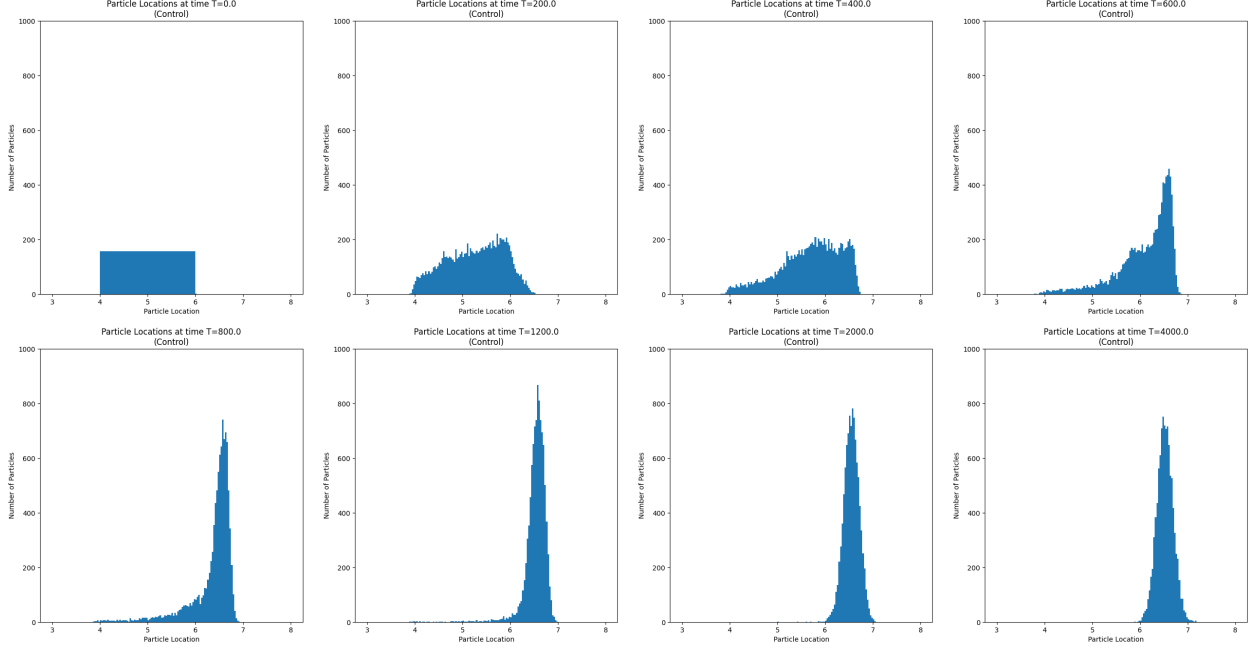


Figure 7.1: Histograms of bacteria locations, with a bin width of 0.04, at equally spaced times  $t$  from  $t = 0$  to  $t = 4000$  in the control simulation (ground truth), i.e., allowing the micro-scale model to run until  $t = 4000$ . We observe that  $t = 4000$  seconds is enough for the system to reach a steady state.

## 7.2 History-Dependent Re-initialization Scheme

To compare with the control data, we perform a simulation using the approximation algorithm with the following parameters:

$S = 200$	length of start-up time
$k = 80$	number of centered differences to average
$H = 95$	length of each approximating step
$H_R = 100$	recovery time after each approximating step
$N_T = 19$	number of approximating steps
$R = 0$	length of additional recover time after last approximating step.

After each approximating step, we re-initialize the underlying data according to the history-dependent scheme in Table 7.4. For example, given data at time  $t_0$ , we use the optimal transport approximation scheme to predict the bacteria locations at  $t_0 + H$ , and re-initialize the microscopic properties at  $t_0 + H$  as follows:

- set  $u_1 = 0$  for all bacteria
- compute  $\left. \frac{du_2}{dt} \right|_{t=t_0}$  from the prescribed ODE in [29] to take an Euler forward step

$$\tilde{u}_2(t_0 + H) := u_2(t_0) + H \cdot \left. \frac{du_2}{dt} \right|_{t=t_0}$$

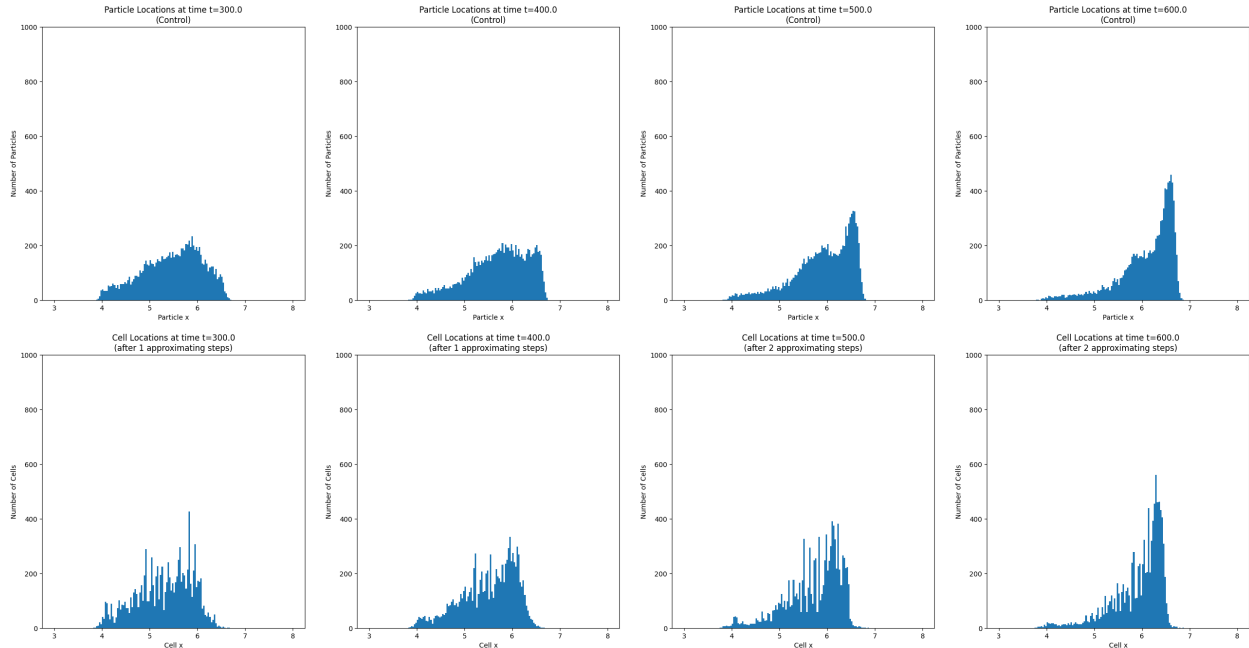


Figure 7.2: Histograms of bacteria locations after the first two approximating steps (bottom) compared with corresponding control simulation (top) (bin size is 0.04). We run the micro-scale simulation until  $t = 200$  (not pictured), approximate to  $t = 300$  (left-most), recover until  $t = 400$  (second from left), then approximate to  $t = 500$  (second from right), and recover until  $t = 600$  (right-most).

- keep the flagella rotating direction and bacteria moving direction exactly the same as they were at time  $t_0$ .

Figures 7.2 and 7.3 show qualitative comparisons between the control simulation and approximation via histograms of the bacteria locations after the first two and last two approximating steps compared with the control data.

### 7.3 Comparison with Different Re-initializations

To demonstrate the effectiveness of the suggested re-initialization, we also perform a history-independent re-initialization as described in [29]. Table 7.4 shows the different parameters of re-initialization between the two schemes. In Figure 7.5, we provide a comparison of the  $W_2$  distance between the control and approximated distributions over time for the two different approximation schemes.

The first approximating step shows similar results between the two experiments while the history-independent scheme becomes (qualitatively good but) “relatively” inaccurate by the end of the first recovery period. This is because the history-independent method re-initializes the microscopic properties with a “fixed” value regardless of current conditions, resulting in a large recovery time to reach slow dynamics while the history-dependent scheme uses the current microscopic properties to re-initialize the next approximating step. In other words, the underlying variables (particularly  $u_2$  and the flagella rotating direction) could not respond quickly enough to the fixed re-initialization. Furthermore, even though the distributions look the same after the first approximation step, the

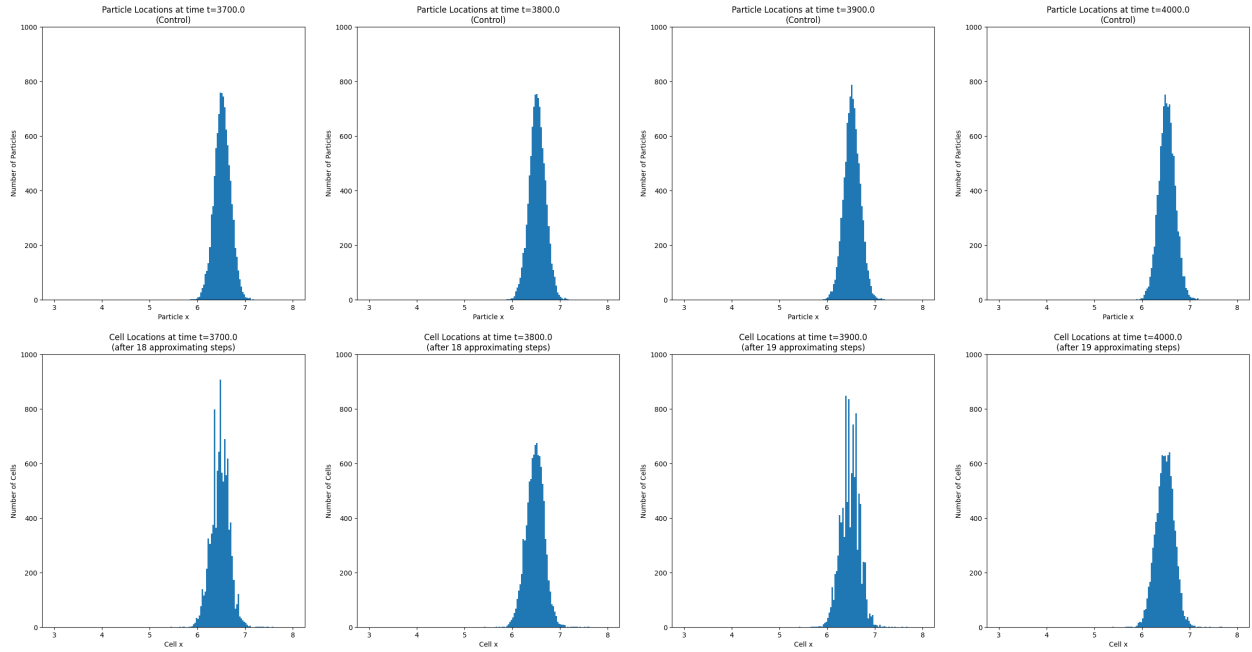


Figure 7.3: Histograms of bacteria locations after the final two approximating steps (bottom) compared with corresponding control simulation (top) (bin size is 0.04). We use data at  $t = 3600$  (not pictured) to approximate to  $t = 3700$  (left-most), recover until  $t = 3800$  (second from left), then approximate to  $t = 3900$  (second from right), and recover until  $t = 4000$  (right-most), the end time.

Parameters	History-Dependent Scheme	History-Independent Scheme
$u_1$	$\tilde{u}_1(t_0 + H) := 0$	$\tilde{u}_1(t_0 + H) := 0$
$u_2$	$\tilde{u}_2(t_0 + H) := u_2(t_0) + H \cdot \left. \frac{du_2}{dt} \right _{t=t_0}$	$\tilde{u}_2(t_0 + H) := f(S(\tilde{x}(t_0 + H)))$
$s^{(i)}$	$\tilde{s}^{(i)}(t_0 + H) := s^{(i)}(t_0)$	$\tilde{s}^{(i)}(t_0 + H) := 0$ (fixed)

Table 7.4: Parameters of different re-initialization schemes. The “history-dependent” scheme (as suggested in this paper) retains the flagella states from the micro-scale simulation immediately before the approximating step, and it attempts to predict  $u_2$  via an Euler forward step. The “history-independent” scheme (as described in [29]) sets a fixed number of flagella to rotate counterclockwise (here, 0), and  $u_2$  is set solely as a function of the predicted location of bacteria.

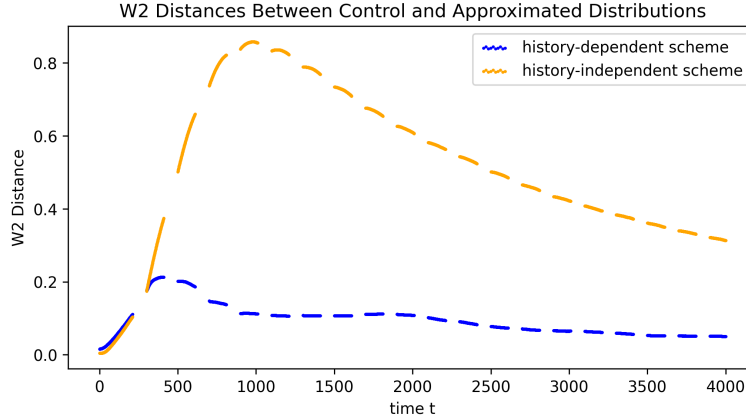


Figure 7.5: For each of the two different re-initialization methods, we compute  $W_2(\mu_t^N, \tilde{\mu}_t^N)$ , the 2-Wasserstein distance between the control distribution  $\mu_t^N$  and the approximate distribution  $\tilde{\mu}_t^N$ . We plot these values at all times  $t$  for which an approximate distribution exists (recall that the point of the approximation algorithm is that we can skip forward in time, so not all times have corresponding approximate distributions). We notice that the history-dependent method outperforms the history-independent method, indicating the importance of re-initializing the underlying variables accurately.

two methods still yield different subsequent microscopic behavior, leading to slightly different slow dynamics.

The observation in Figure 7.5 suggests that the underlying microscopic properties are important components in the micro-scale simulation. Hence, different settings of the properties result in different overall distribution behavior. In the language of Section 4, the vector field that describes the distribution evolution is somehow a function of these variables, not merely a function of position, so the method we choose to predict them across approximating steps is critical to our capability to approximate the evolution using optimal transport maps.

We demonstrate that both schemes show the convergence to the controlled simulation within the error bounds. This observation shows that the re-initialization of microscopic properties quickly diverges slow dynamics but some schemes work better for particular problems. Here, the history-dependent scheme, which retains the flagella states from the previous step, better allows the distribution to continue moving at the same speed. In this experiment, since we used the Gaussian distribution of chemoattractant which has a smooth change of its derivative, the change of rotating direction over time is not a normal event. Hence, keeping the same states provides us with better initialization. For the same reason, imposing the Euler forward step of  $u_2$  may guarantee that the approximation is near the controlled simulation, see Figure 7.6.

Like all mathematical models, choices about which prediction methods should be used depend entirely on the needs of the particular application. Unfortunately, these choices are mostly ad hoc and context-specific, so there is little to say in general about how they impact the accuracy of the overall approximation algorithm.

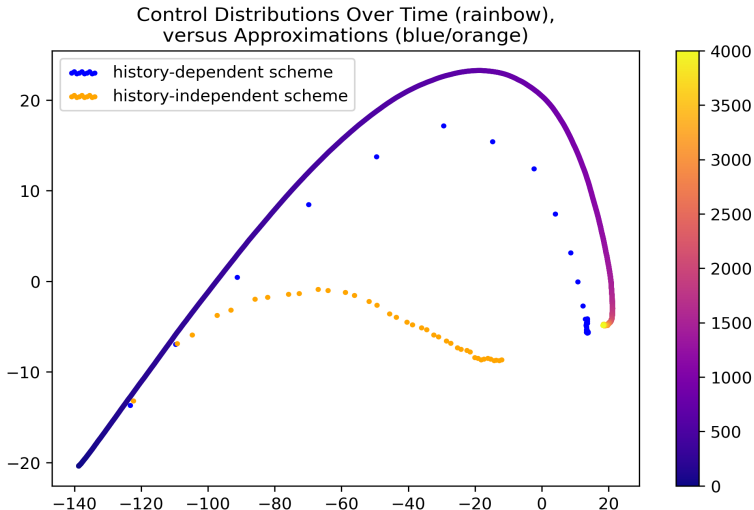


Figure 7.6: Plot of the first two principal components of the control distribution evolution at different times (solid rainbow curve). Color bar to the right represents time from  $t = 0$  to  $t = 4000$ . Also plotted are the projections of the two different approximation schemes at intervals of  $t = 100$  (after each approximating step and each recovery period). We see that the history-dependent re-initialization method more closely tracks the control distribution’s evolution despite the two methods producing nearly identical first approximations (near  $(-115, -5)$  on the plot), once again indicating the importance of re-initializing the underlying variables accurately.

## 8 Conclusions and Future Work

While the proposed prediction algorithm is only theoretically guaranteed to be accurate for continuous measures, the experiments we have performed indicate that it does indeed work on discrete measures (e.g., particle systems) as well. This suggests that there is a discrete analog to Theorem 4.6 that will guarantee accuracy, although the result will certainly need more care due to the subtlety in choosing an appropriate time step  $h$ . Nonetheless, optimal transport is a promising direction in the development of new multiscale modeling and projective integration techniques. It is not yet clear whether an optimal transport approach will be competitive with the state of the art time stepping methods, but it does nicely generalize some previously proposed ideas.

We have mentioned some theoretical directions for further work throughout the paper, but there are also many experimental ideas for improving the algorithm. Some of these rely on the development of new theory (e.g., adapting the length of the approximating step based on an estimate of a second derivative in Wasserstein space), but some are based on practical methods from other areas. One easy extension is to use a kernel smoothing technique to reduce the noise in the approximated distributions and thus allow for reduced recovery times. Another natural extension is to use the idea behind telescopic projective integration [10] to develop an algorithm for modeling systems that have more than two distinct time scales. Our proposed algorithm is only practical if the length of the approximating step is a significant fraction of the end time of interest, but this may not be true for more complicated multi-scale systems. In such cases, we would need an algorithm that takes medium-length approximating steps and computes an approximation for an even-more substantial time in the future.

## References

- [1] Luigi Ambrosio and Nicola Gigli. *A User's Guide to Optimal Transport*, pages 1–155. Springer Berlin Heidelberg, Berlin, Heidelberg, 2013.
- [2] Luigi Ambrosio, Nicola Gigli, and Giuseppe Savaré. *Gradient Flows in Metric Spaces and in the Space of Probability Measures*. Lectures in Mathematics ETH Zürich. Birkhäuser, 2. ed edition, 2008. OCLC: 254181287.
- [3] Jean-David Benamou and Yann Brenier. A computational fluid mechanics solution to the Monge-Kantorovich mass transfer problem. *Numerische Mathematik*, 84(3):375–393, 2000.
- [4] Yann Brenier. Polar factorization and monotone rearrangement of vector-valued functions. *Communications on Pure and Applied Mathematics*, 44(4):375–417, 1991.
- [5] Alexander Cloninger, Keaton Hamm, Varun Khurana, and Caroline Moosmüller. Linearized Wasserstein dimensionality reduction with approximation guarantees. *arXiv preprint arXiv:2302.07373*, 2023.
- [6] Weinan E and Bjorn Engquist. The heterogeneous multiscale methods. *Communications in Mathematical Sciences*, 1(1):87 – 132, 2003.
- [7] Weinan E, Di Liu, and Eric Vanden-Eijnden. Analysis of multiscale methods for stochastic differential equations. *Communications on Pure and Applied Mathematics*, 58(11):1544–1585, 2005.
- [8] C. W. Gear, D. Givon, and I. G. Kevrekidis. Virtual slow manifolds: The fast stochastic case. *AIP Conference Proceedings*, 1168(1):17–20, 09 2009.
- [9] C. W. Gear and Ioannis G. Kevrekidis. Projective methods for stiff differential equations: Problems with gaps in their eigenvalue spectrum. *SIAM Journal on Scientific Computing*, 24(4):1091–1106, 2003.
- [10] C.W Gear and Ioannis G Kevrekidis. Telescopic projective methods for parabolic differential equations. *Journal of Computational Physics*, 187(1):95–109, 2003.
- [11] C.W. Gear, Ioannis G. Kevrekidis, and Constantinos Theodoropoulos. ‘Coarse’ integration/bifurcation analysis via microscopic simulators: micro-Galerkin methods. *Computers & Chemical Engineering*, 26(7):941–963, 2002.
- [12] Nicola Gigli. On Hölder continuity-in-time of the optimal transport map towards measures along a curve. *Proceedings of the Edinburgh Mathematical Society*, 54(2):401–409, 2011.
- [13] Somdatta Goswami, Aniruddha Bora, Yue Yu, and George Em Karniadakis. Physics-informed deep neural operator networks. In *Machine Learning in Modeling and Simulation: Methods and Applications*, pages 219–254. Springer, 2023.
- [14] Somdatta Goswami, Katiana Kontolati, Michael D Shields, and George Em Karniadakis. Deep transfer operator learning for partial differential equations under conditional shift. *Nature Machine Intelligence*, 4(12):1155–1164, 2022.

- [15] Guillaume Hugué, D Magruder, Alexander Tong, Oluwadamilola Fasina, Manik Kuchroo, Guy Wolf, and Smita Krishnaswamy. Manifold interpolating optimal-transport flows for trajectory inference. *Advances in neural information processing systems*, 35:29705–29718, 12 2022.
- [16] Ioannis G. Kevrekidis, C. William Gear, and Gerhard Hummer. Equation-free: The computer-aided analysis of complex multiscale systems. *AIChE Journal*, 50(7):1346–1355, 2004.
- [17] Ioannis G. Kevrekidis, C. William Gear, James M. Hyman, Panagiotis G Kevrekidis, Olof Runborg, and Constantinos Theodoropoulos. Equation-Free, Coarse-Grained Multiscale Computation: Enabling Microscopic Simulators to Perform System-Level Analysis. *Communications in Mathematical Sciences*, 1(4):715 – 762, 2003.
- [18] Nikola B Kovachki, Samuel Lanthaler, and Hrushikesh Mhaskar. Data complexity estimates for operator learning. *arXiv preprint arXiv:2405.15992*, 2024.
- [19] Seungjoon Lee, Yorgos M. Psarellis, Constantinos I. Siettos, and Ioannis G. Kevrekidis. Learning black- and gray-box chemotactic pdes/closures from agent based Monte Carlo simulation data. *Journal of Mathematical Biology*, 87(1):15, 2023.
- [20] G. Loeper. On the regularity of the polar factorization for time dependent maps. *Calculus of Variations and Partial Differential Equations*, 22(3):343–374, 2005.
- [21] John Lott. Some geometric calculations on Wasserstein space. *Communications in Mathematical Physics*, 277:423–437, 01 2008.
- [22] Lu Lu, Pengzhan Jin, Guofei Pang, Zhongqiang Zhang, and George Em Karniadakis. Learning nonlinear operators via DeepONet based on the universal approximation theorem of operators. *Nature machine intelligence*, 3(3):218–229, 2021.
- [23] Quentin Mérigot, Alex Delalande, and Frédéric Chazal. Quantitative stability of optimal transport maps and linearization of the 2-Wasserstein space. In Silvia Chiappa and Roberto Calandra, editors, *Proceedings of the Twenty Third International Conference on Artificial Intelligence and Statistics*, volume 108 of *Proceedings of Machine Learning Research*, pages 3186–3196. PMLR, 2020.
- [24] Hrushikesh N Mhaskar. Local approximation of operators. *Applied and Computational Harmonic Analysis*, 64:194–228, 2023.
- [25] Caroline Moosmüller and Alexander Cloninger. Linear optimal transport embedding: Provable Wasserstein classification for certain rigid transformations and perturbations, 2021.
- [26] Felix Otto. The geometry of dissipative evolution equations: The porous medium equation. *Communications in Partial Differential Equations*, 26(1-2):101–174, 2001.
- [27] Gabriel Peyré and Marco Cuturi. Computational optimal transport. *Foundations and Trends in Machine Learning*, 11(5-6):355–607, 2019.
- [28] Filippo Santambrogio. *Optimal Transport for Applied Mathematicians*. Progress in Nonlinear Differential Equations and Their Applications. Birkhäuser Cham, 2015.
- [29] S. Setayeshgar, C. W. Gear, H. G. Othmer, and I. G. Kevrekidis. Application of coarse integration to bacterial chemotaxis. *Multiscale Modeling & Simulation*, 4(1):307–327, 2005.

- [30] Alexander Tong, Jessie Huang, Guy Wolf, David Dijk, and Smita Krishnaswamy. Trajectory-net: A dynamic optimal transport network for modeling cellular dynamics. *Proceedings of machine learning research*, 119:9526–9536, 07 2020.
- [31] Eric Vanden-Eijnden. Numerical techniques for multi-scale dynamical systems with stochastic effects. *Communications in Mathematical Sciences*, 1(2):385–391, 2003.
- [32] Wei Wang, Dejan Slepčev, Saurav Basu, John A. Ozolek, and Gustavo K. Rohde. A linear optimal transportation framework for quantifying and visualizing variations in sets of images. *International Journal of Computer Vision*, 101(2):254–269, 2013.
- [33] Yewei Xu and Qin Li. Forward-euler time-discretization for wasserstein gradient flows can be wrong, 2024.